UNIVERSITY OF OKLAHOMA

GRADUATE COLLEGE

PROBE-BASED, QUASI-NEAR-FIELD PHASED ARRAY CALIBRATION

A DISSERTATION

SUBMITTED TO THE GRADUATE FACULTY

in partial fulfillment of the requirements for the

Degree of

DOCTOR OF PHILOSOPHY

By

SHAJID ISLAM
Norman, Oklahoma
2020

PROBE-BASED, QUASI-NEAR-FIELD PHASED ARRAY CALIBRATION

A DISSERTATION APPROVED FOR THE
SCHOOL OF ELECTRICAL AND COMPUTER ENGINEERING

BY THE COMMITTEE CONSISTING OF

Dr. Caleb Fulton, Chair

Dr. Mark Yeary

Dr. Joseph Havlicek

Dr. Hjalti Sigmarsson

Dr. Javier Alejandro Chávez-Domínguez

© Copyright by SHAJID ISLAM 2020
All Rights Reserved.

To my parents, Rafiqul Islam and Rebeka Sultana, for the unconditional love and support and to my wife, Rowzat Faiz, for believing in me.

Acknowledgments

Getting into the graduate program was not an easy decision for me when I finished my undergraduate study in Bangladesh. A good number of people helped me throughout this journey, and this is the chance to express my gratitude towards them. I want to begin by thanking three influential friends in my life, Tanvir Obaid, Ishtiaqe Noor, and Ehsanul Karim, for their support when I needed it the most. I would also like to acknowledge my friend Taufique Atique for his constant moral support throughout my Ph.D.

I owe a tremendous debt to my family that has supported me through this journey. My parents helped me in every way possible through the years, and no thanks will ever be sufficient for that. The sacrifice they made to support my endeavor is incredible. I am incredibly grateful to my wife, Rowzat Faiz, for everything she has done in my life. The journey towards Ph.D. is difficult, but without her unconditional support, it would be almost impossible. Thank you.

Collins Aerospace supports this research, and I met some wonderful people while working with them. Dr. Lee Paulsen offered an extraordinary level of support and guidance to me from the beginning of my Ph.D. till the end. I am indebted to him for all his mentoring throughout the process. I would also like to thank Connor McBryde, Orion Davies, and Jon Lovseth for making my internship experience meaningful. I also wish to extend special thanks to my fellow Ph.D. students and friends, Dr. Rodrigo Lebron, Dr. Robin Irazoqui, Dr. Andrew Byrd, and Dr. Nicholas Peccarelli.

Finally, Dr. Caleb Fulton, my Ph.D. advisor and mentor (both technical and otherwise); who has shaped me into the person I am today for the last five years. Dr. Fulton is a model of extraordinary depth and breadth of technical

brilliance, and at the same time, he posses the rare quality of how to make engineering work enjoyable. I am sure most people at ARRC really enjoy what they do, but Dr. Fulton looks at things way differently and makes you no choice but to have fun. Working for Dr. Fulton is a great experience and truly been a privilege. I can undoubtedly declare that Celeb is one of the smartest person I ever met. I am also grateful to my committee members as they always accommodate and guide me when needed.

Table of Contents

List of Tables

List of Figures

ABSTRACT

Phased array technology provides remarkable scanning flexibility and spatial search capability for the multifunction radar system, airborne radar system, and many other applications. Recent years have seen a noticeable surge towards low cost, small phased array antenna technology in a varied range of sectors due to its diverse applicability. However, lowering the cost exposed phased array antenna to various errors, among which excitation errors, such as incorrect phase and amplitude, is one of the major concerns. Excitation errors affect essential performance parameters such as side-lobe level, antenna gain, active impedance, and beam-forming quality. It is crucial to quantify and compensate for the errors associated with each antenna element's phase and amplitude to ensure the phased array antenna's desired performance. The process of this compensation is widely known as the calibration of a phased array. The diverse application and increased use of a low cost small phased array system make the front end calibration procedure very challenging. This challenge is two-fold. The calibration should be done accurately and quickly as possible. This dissertation focuses on developing a novel technique of phased array calibration using a fixed probe in the quasi-near-field of the antenna. The objective is to significantly reduce calibration time and associated cost without compromising the calibration quality for initial and in-situ calibration. After the development of a successful mathematical framework, a detailed simulation is conducted to analyze the system. The proposed technique was finally validated using an active electronically scanned array inside a custom-made compact range and near field range.

Chapter 1

INTRODUCTION

Phased array radar and communication systems have advanced significantly in recent years. The ability to have high gain with low side-lobes, beam steering, multifunction operation, emission of several beams simultaneously, and adaptability makes phased array antennas more popular. Now researchers are trying to take it a step further. The goal is to provide low cost, low weight, and small-sized phased array antennas without compromising the system's flexibility and functionality, as described in [1–3]. One of the critical features of phased array antennas is electronic beam steering, which is achieved by adjusting the phase of the signal received or transmitted by each antenna element. The signals from every element become in phase for a specific beam scan angle desired for beam steering. The amplitude also plays a vital role in controlling side-lobes and optimizing aperture efficiency. The amplitudes and phases of the element channels relative to each other determine the shape of the antenna pattern.

Due to manufacturing variability and unavoidable natural phenomenon, there is often considerable deviation in relative phase and amplitude of the

elements from their desired values. A multitude of reasons causes this. It might be coming from attenuators, amplifiers, dividers, combiners, switches, connectors, or transmission lines such as coaxial cables and waveguides. Secondary parameters such as temperature and pressure are also responsible for drifts in phase and amplitude of the elements. Digital arrays have even more source of errors from oscillators and amplifiers. To address these issues and ensure that the phased array antenna is working correctly, it is essential to calibrate the antenna by measuring and equalizing all element channels' phase and amplitude effects.

1.1 Problem Statement and Motivation

The complex excitation (phase and amplitude) of the element channels relative to each other determines the shape of the antenna pattern. There is often considerable deviation in the relative phase and amplitude values compared to the desired values, as explained in [4–7], for various reasons; these can be defined as excitation errors. They might be caused by a different combination of error sources, as mentioned earlier.

There are a wide variety of calibration procedures available for different system types, such as those that use analog beamforming, hybrid beamforming, or full digital beamforming. After the array is fabricated, a suitable calibration procedure is performed for different frequencies, temperatures, and other operational conditions to compensate for various errors and ensure system performance. This process is known as "initial calibration" throughout the dissertation, focusing on element-level amplitude and phase alignment in the RF front end. Without this initial calibration, a phased array antenna is unlikely to meet its performance goals.

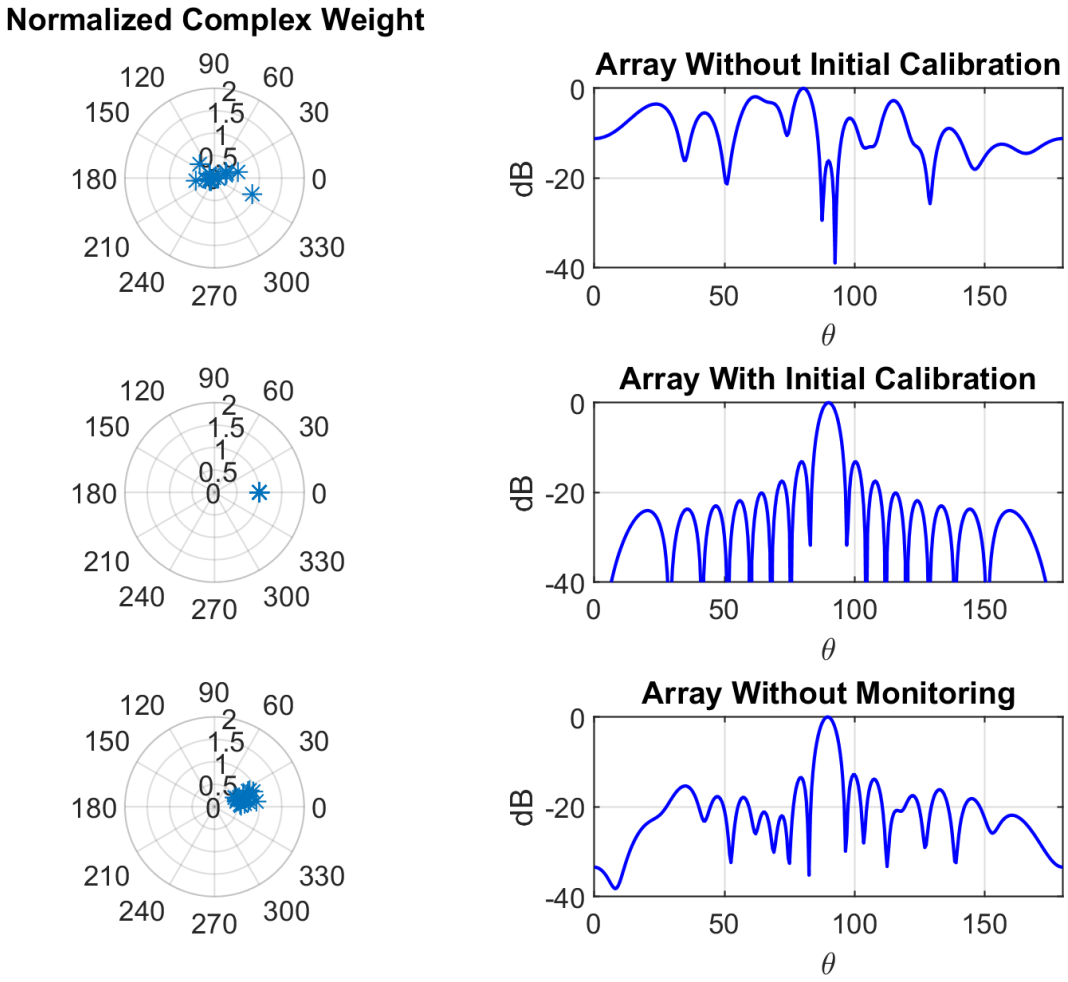

Figure 1.1: Typical pattern of a 16 element Uniform Linear Array (ULA) in three different stages: 1) without any calibration; 2) with initial calibration; and 3) after subsequent errors without any monitoring

In Figure 1.1, a typical 16 element $\frac{\lambda}{2}$ dipole, half-wavelength spacing, uniform linear array pattern is plotted. First, the pattern is plotted without initial calibration. This includes manufacturing and random errors. It can be observed that the pattern without initial calibration is almost of no use. Then a well-calibrated pattern is also plotted to emphasize the impact of ideal initial calibration.

After the initial calibration, when the array is deployed for its operation, secondary parameters such as component aging, change in environment, and

component failure often affect the antenna. Different performance monitoring techniques are available while the array is fielded to address this problem. In Figure 1.1, the last pattern showed the unmonitored pattern condition. It is visible how the pattern started to deviate from the ideal shape without any monitoring.

The first step of calibrating a phased array is often finding out how each element radiates at a specific frequency and how the control of each element translates into phase and amplitude in the far-field. The next step typically involves a rigorous investigation of secondary parameters such as temperature, power supply loading, humidity, etc., which can affect each element's behavior. During this process, some critical assumptions will play a significant role. A linear relationship is often assumed between an element's complex element-level control and the amplitude and phase of the signal received/radiated by that element given a constant set of secondary parameters. This assumption is accurate for digital phased arrays where phase shifting is done digitally, and every element has its own transmit and receive (T/R) module. However, in analog beamforming architectures, the complex excitation controllers suffer from phase ripple errors, deviation in the quantization stage, and change in phase while attenuating the signal. Still, this linear relationship is often assumed throughout the literature, as discussed in Section 2.2. However, it is customary to check if any of these variations are significant enough to violate this assumption during the initial calibration procedure.

The ideal first-order approximation of radiation pattern for the phased array is defined as the product of "array factor" and "element factor." Many factors can impact this approximation, such as mutual coupling, finite array effects, corner element effects, and embedded element patterns. Stutzman

and Kelley [8] showed a good overall pattern modeling which includes mutual coupling. They showed that the overall pattern of an array is expressed as

$$E(\theta, \phi) = \sum_{n=1}^{N} A_n F_n(\theta, \phi) \ , \tag{1.1}$$

where E is the overall array pattern, A_n is the desired current or voltage (depending on the element and model) at the element excitation port, and F_n is defined as an individual element pattern. All effects such as finite array edge effects, element positions, electrical and mechanical variations between elements, and mutual coupling are lumped into this pattern. For validation purposes, one has to take all the elements measured individually and fit a model that follows the equation 1.1 to synthesize the overall pattern. For example, THAAD [9] (Theater High Altitude Area Defense) radar had to go through 25344 T/R modules near-field scanned individually for different settings of phase state. Once the antenna position and element excitation is determined, the only variation in the individual element pattern needs to be investigated. For a large array consisting of several hundreds or thousands of elements, most of the elements are positioned away from the edge. Though the edge elements still see the discontinuity in the array's periodicity, the overall effect of that discontinuity is not highly impactful on the total array pattern. Therefore, it is often safe to assume that all elements in such an array have the same pattern shape. The overall pattern can be denoted by rewriting equation 1.1 as

$$E(\theta, \phi) = F_0(\theta, \phi) \sum_{n=1}^{N} w_n A_n e^{jk \cdot r_n}, \tag{1.2}$$

where A_n is the static gain and phase of the n^{th} channel, r_n is the location of n^{th} element, w_n is the complex weight of the n^{th} channel and $F_0(\theta, \phi)$ is

the general individual element pattern under the previous assumption that it varies insignificantly throughout the array. It is important to note that in large arrays, this pattern can describe fundamental behavior including any array blindness [10] and effects associated with active impedance [11]. After factoring out the general element pattern from the equation, the calibration goal is to generate the desired $I_n = w_n A_n$ values for beam synthesis. This overall process relies on what is known as the large array approximation, where all elements are assumed to have the same embedded pattern. This large array approximation cannot be used for small arrays because of edge effects.

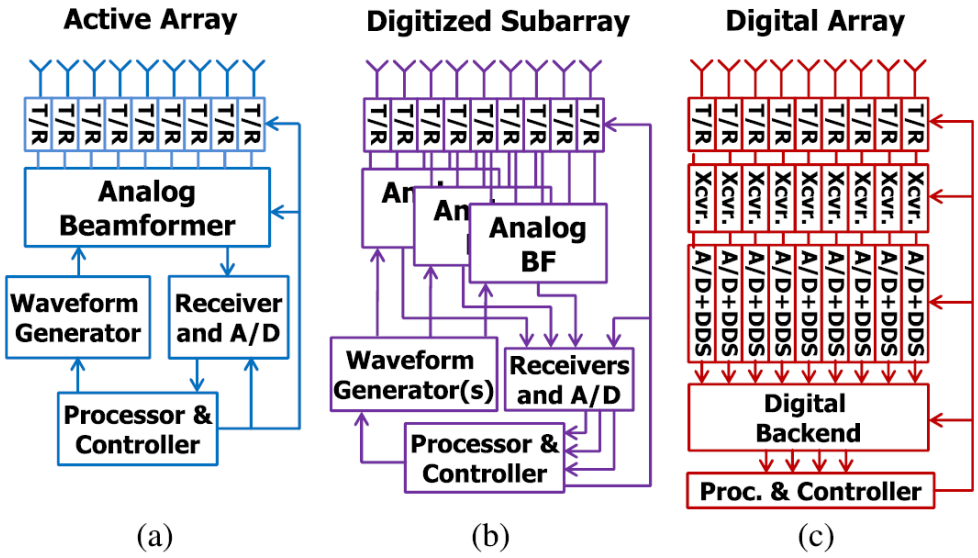

Figure 1.2: Generic beamforming architecture; a) traditional analog beamformer, b) hybrid beamformer c) full digital beamformer.
Source: [17]

The dominant criteria for selecting one method largely depends on the array architecture, size, and available instrumentation. In Figure 1.2(a), a traditional analog beamforming architecture is depicted where it may have solid-state front end electronics. Figure 1.2(b) shows, a modern digitized sub-

array with multiple digital transceiver modules. Finally, in Figure 1.2(c), a fully digital array architecture is displayed with digital transceiver modules in each element. Irrespective of what architecture has been used, each of them required initial calibration and in-situ monitoring. It is also worthy to note that sampling only excitation errors will not guarantee a thorough assessment of the array performance; we also need to evaluate the resulting beam pattern to ensure a well-calibrated array. From an antenna engineer's point of view, given the architectural differences of the three different arrays in Figure 1.2, it is challenging to provide a single calibration solution that will work for every type of phased array.

Though calibration of a phased array is an essential part of a phased array system, no universally accepted calibration technique is available due to many underlying factors such as array design, requirements, array size, available instrumentation, etc. The calibration technique literature is vast and varied widely due to the diversity of system needs and available resources in the history of open phased array related publications. Moreover, there is no commercially available equipment dedicated for calibration purposes only. The traditional instrumentation needed to calibrate a phased array is a probe, a vector network analyzer (VNA) or some sort of synchronized transmitter/receiver, and typically an anechoic chamber. An antenna near-field range is a good fit for calibration purposes since it can perform sampling and pattern measurement automatically. However, with the diversity of modern phased array systems and technologies, near-field ranges are not always the right solution for low-cost, fast calibration for several reasons. First, these ranges are not explicitly designed for calibration purposes. So, they typically require both software and hardware developments to enable calibration. Secondly, these

antenna ranges are typically large, not mobile, and require special supervision to maintain the environment. Another major disadvantage with the available calibration techniques is that they take a long time to calibrate a single phased array. Researchers throughout the world are looking to find a fast and accurate calibration method.

In this context, this dissertation will focus on the fundamentals of phased array antenna calibration; it focuses on different calibration techniques available, discusses advantages and disadvantages of those techniques, and proposes a novel approach that can offer a fast calibration method for certain modern phased array architectures, especially those that cannot be calibrated using with external equipment once they have been fielded, for practical reasons.

1.2 Research Scope

Phased array calibration is a broad term used to describe several techniques and procedures for ensuring that each element's amplitude and phase are set correctly, as a function of frequency, temperature, and more. This can involve establishing and enforcing a wide range of control parameters, such as proper magnetic material current biases for older phased arrays that use ferrite phase shifters (e.g., the SPY-1) or, in modern digital phased arrays, nonlinear equalization pre-/post-distortion. One must also note that there are at least two distinct stages to general calibration: 1) initial calibration, performed during factory testing in, for example, an anechoic chamber, and 2) in-situ (or on-line), performed using equipment that is fielded with the array (or is built into the array). The efficacy of a given technique is often a vital function of the assumptions underlying the mathematical model from which they are derived, and any deviation from ideal conditions (e.g., array behavior as assumed) will

therefore lead to some amount of residual errors, no matter how carefully the technique is executed.

This dissertation's primary motivation is to provide a novel calibration procedure, which will reduce the calibration time and necessary equipment demand significantly without compromising the calibration performance. The first step is to investigate several relevant modern phased array calibration techniques, paying particular attention to their underlying assumptions and potential pitfalls, to establish a context for more significant developments. Once the survey is complete, the next step is to develop a mathematical framework of the proposed technique on initial calibration using a fixed probe in the quasi-near-field region of the phased array. This framework will ensure the first block of proof of concept of this technology. Based on the development of this mathematical framework, a ®MATLAB toolbox has been created to simulate a ground truth situation for a simple array. The electromagnetics are captured precisely and accurately to provide a reference for analysis of the system. This dissertation is limited to linear, CW (single frequency), single-polarization calibration procedures. The wideband, time-delay effects, array non-linearity, and dual-polarization will be left for future work.

Next, for validation, measurements are shown that were taken using the Advanced Technology group's lab facilities at Collins Aerospace. They provided a proprietary array to validate the proof of concept of the fast calibration technique. This procedure validated the proposed method for quick initial calibration and analyzed the resulting calibration efficacy in a custom-made near-field range. The primary antenna characteristics are also investigated.

1.3 Contribution

This dissertation primarily focuses on a novel calibration technique to reduce the cost and downtime of an active electronically scanned array (AESA) without compromising calibration effectiveness. It first provides a survey of existing calibration procedures and discuss their merits and demerits. Next, it lays out a novel calibration procedure with a mathematical framework and ®MATLAB-based simulation. Finally, it validates the proposed method with measurements in a custom-made chamber and near-field chamber. The key contributions are listed below:

- Development of a novel low -cost, fast calibration technique with a fixed probe in the quasi-near-field, which is capable of performing the calibration procedure quickly while maintaining the calibration standards.
- Development of a mathematical framework and ®MATLAB sandbox to analyze different errors generated from various assumptions to calibrate analog and digital arrays of different sizes and shapes.
- Experimental verification using an electronically scanned array (ESA) using a low-cost custom made range and then in a standard near-field range.
- Development and implementation of a virtual probe location algorithm to avoid random errors related to the probe position.

1.4 Dissertation Outline

This dissertation is comprised of six chapters, including this introduction. Chapter 2 reviews the fundamentals of phased array antennas, emphasizing

some unique characteristics that are different from traditional antennas. It shows array radiation pattern effects due to calibration errors in the context of a proper mathematical framework to understand why calibration is needed. It also emphasizes other calibration procedures widely used by engineers and researchers.

Chapter 3 presents the theory of the proposed calibration technique and discusses how it solves some existing fundamental problems such as cost and calibration speed. It also displays the mathematical framework for the proposed method and how it will work in both analog and digital arrays.

One of the essential aspects of fixed probe-based calibration that is poorly understood is approximating the probe-to-element interactions as being far-field, primarily when a simple point source model is used for the probe's radiation. To better understand this effect and simulate the proposed technique, a ®MATLAB sandbox has been developed; it is presented in Chapter 4. The simulation of the "ground-truth" situation is described. Also, the proposed approach is simulated within this sandbox.

Chapter 5 validates the proposed fast calibration procedure technique with measured data. The system used to validate the method was provided by Collins Aerospace. Some essential phased array characteristics are also shown as a figure of merit to prove the calibration standard's efficacy.

Finally, Chapter 6 summarizes the findings from the experiments and discusses the conclusions. Some prospective future work is also discussed.

Chapter 2

FUNDAMENTALS OF PHASED ARRAY ANTENNA AND CALIBRATION TECHNIQUES

Phased array antennas are defined as a set of multiple stationary antenna elements coherently fed and capable of scanning a beam electronically, to a given angle in space, by using variable time delay or phase control at each element. Pattern shaping can be achieved by using variable amplitude for different elements of the array. The primary reason to use phased arrays is the capability of beam steering. If the antenna elements are chosen carefully, a phased array antenna can steer the main beam to a target direction. The overall performance of a phased array principally depends on three major parameters: the

shape of the array, amplitude and phase of each element, and the radiation pattern of each element. Also, the antenna has to be impedance matched well within its operating frequency for optimal performance. Some of the advantages of using phased arrays are that they have electronic beam steering capabilities, offer flexible directivity, and can generate multiple beams simultaneously, which makes them proper candidates for surveillance and tracking in radar. According to [31], the overall pattern of a phased array antenna can be controlled using five variables. These are,

- The geometrical arrangement of the phased array elements
- The relative gap between the elements
- The excitation amplitude of each element
- The excitation phase of each element
- The individual element pattern.

Each of the criteria mentioned above has a significant impact on the phased array antenna's overall performance. However, the amplitude and phase controls are typically the only variables that are able to be changed for each scan angle during normal operation.

2.1 Fundamentals of Phased Array

2.1.1 Pattern Synthesis Equation

Two typical configurations of the phased array will be considered for analysis. Figure 2.1 depicts the usual linear and planar phased array geometries. Generally, each element's complex excitation weight (amplitude and phase)

is controlled by attenuators and phase shifters. In addition to the complex weight on each element, a relative phase shift is observed between waves arriving at (or departing from) each element due to the element's position in space and the wave's angle of arrival (or departure). The array's radiation pattern will be the superposition of all fields/responses from each antenna element. To examine a simple linear N-element phased array antenna, let us take $f_n(\theta, \phi)$ as a representative of the n th element's far-field (FF) radiation pattern, as a function of elevation angle θ and azimuth angle ϕ in spherical coordinates, keeping the origin in the center of the antenna element.

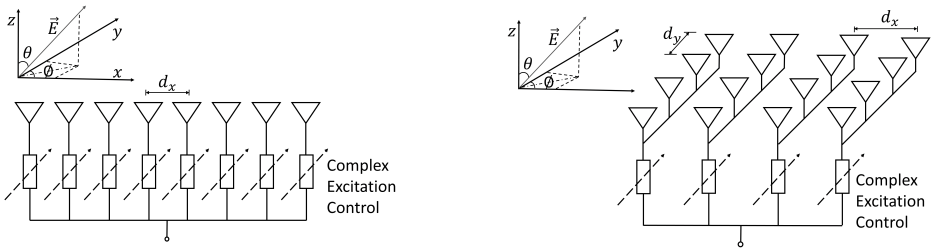

(a) Linear array configuration (b) Planar array configuration

Figure 2.1: Typical linear and planar configuration of equally spaced phased array

Then, the array radiation pattern will be the summation of all elements' individual patterns $f_n(\theta, \phi)$ with a phase shift due to each element's spatial offset from the phase center. It can be mathematically expressed as [32]

$$f(\theta, \phi) = \sum_{n=1}^{N} f_n(\theta, \phi) e^{-jk\hat{\mathbf{r}} \cdot \mathbf{r_n}} \ , \tag{2.1}$$

where $f(\theta, \phi)$ is the overall pattern of the full array. The wavenumber is defined as $k = \frac{2\pi}{\lambda}$ where λ is the wavelength of the signal. Now, $\hat{\mathbf{r}}$ is a unit vector in the direction of observation point, defined as

$$\hat{\boldsymbol{r}} = \sin\theta\cos\phi\hat{\mathbf{x}} + \sin\theta\sin\phi\hat{\mathbf{y}} + \cos\theta\hat{\mathbf{z}} \ , \tag{2.2}$$

and $\mathbf{r_n}$ is the position vector of each element from the center of the array. Now if we add the complex weight to manipulate the amplitude and phase of each of the element, then equation 2.1 becomes

$$f(\theta,\phi) = \sum_{n=1}^{N} w_n f_n(\theta,\phi) e^{-jk\hat{\mathbf{r}}\cdot\mathbf{r_n}} \ , \tag{2.3}$$

where

$$w_n = a_n e^{j\psi_n} \ , \tag{2.4}$$

w_n is the amplitude excitation of each element, and ψ_n is the progressive phase excitation of the corresponding element. Typically in an analog active electronically scanned array, the complex weight w_n realized by the TR module of the n th element using phase shifters and attenuators. Often researchers assume that all radiating elements share the same embedded element pattern, which makes equation 2.3

$$f(\theta,\phi) = f_0(\theta,\phi) \sum_{n=1}^{N} w_n e^{-jk\hat{\mathbf{r}}\cdot\mathbf{r_n}} \ , \tag{2.5}$$

where $f_0(\theta,\phi)$ is used as common radiation pattern for each element. In the context of calibration, the complex excitation w_n plays an important role. In general, the amplitude distribution a_n of the elements controls the beam shape of the pattern, and the phase excitation ψ_n is responsible for pointing the direction of the main beam. Hence, if we want to set our antenna pattern in our desired shape and direction, we have to choose the value of w_n wisely. We can also look at w_n as actuators that compensate for the different errors introduced

by the system's RF components. This dissertation focuses on finding the complex excitation weights to generate our desired beam.

2.1.2 Influence of Excitation Errors

The precision of phased array excitation has been reduced as various random and spatially correlated errors are introduced across the array of defective components and signal distribution networks. Some of the familiar error sources are listed in Table 2.1.

Mechanical	**Environmental**	**Electrical**
Manufacturing Errors	Temperature	Components
Misalignment assembly	Rain/Snow	VSWR
Distortion due to stress	Wind variation	T/R module
	Multi-path	Material tolerances
	EMI	Radome errors
		Surface tolerences
		Element Outage
		Thermal noise

Table 2.1: List of mechanical, environmental and electrical error source within RF chain

We can divide array errors into two broad categories: systematic and random, as stated by [7] and [34]. Systematic errors are also known as correlated errors, including periodic phase and amplitude errors caused by discrete phase shifters, amplitude attenuation errors across the array, and frequency-dependent phase errors due to contiguous wideband subarrays with time delay.

There are no general rules to mitigate systematic errors because they can appear in different types and combinations. Systematic errors are generally more impactful than random errors. In a well designed and manufactured phased array where element position and orientation errors are small, it is possible to remove all correlated errors. The array is prone to random phase and amplitude errors only. These errors are treated as random errors, impacting directivity reduction, side-lobe level change, and beam pointing error. These errors are estimated using statistical procedures. In the developments for this present work, all random errors will be assumed normally distributed with zero mean and have a variance of σ^2.

Before diving to the further details, it is necessary to define the variances that will quantify the excitation errors. The literature defines the root mean squared error (RMSE), also known as standard deviation errors, for phase, σ_ϕ and for amplitude, σ_{amp}. In mathematical terms they are defined as

$$\sigma_\phi = \sqrt{\frac{1}{N}\sum_{n=1}^{N} |\phi_n - \phi_n^T|^2} \ , \tag{2.6}$$

and

$$\sigma_{amp} = \sqrt{\frac{1}{N}\sum_{n=1}^{N} \left(\frac{|A_n - A_n^T|}{A_n^T}\right)^2} \ . \tag{2.7}$$

Here, N is the total number of elements in the array, ϕ_n and ϕ_n^T are the actual phase excitation and target phase excitation of nth element, respectively. Similarly, A_n and A_n^T are the realized and target amplitude of the n th element.

2.1.2.1 Average Side-lobe Level

Let us consider a linear array of half wavelength spacing isotropic elements, where the space factor is

$$f_0(u) = \sum A_n e^{jn\pi u} \ ; \tag{2.8}$$

with the addition of errors, the coefficient A_n becomes

$$A_n(1 + \delta_{amp})e^{j\delta_\phi} \ , \tag{2.9}$$

where amplitude error $\delta_{amp,n} = (A_n - A_n^T)$, and phase error $\delta_{\phi,n} = \phi_n - \phi_n^T$. So the array power pattern now becomes [34]

$$f^2 = \sum \sum A_n A_m^* (1 + \delta_{amp,n})(1 + \delta_{amp,m}) e^{j(\delta_{\psi,n} - \delta_{\psi,m} + (n-m)\pi u)} \ . \tag{2.10}$$

Considering the assumptions mentioned earlier, we can define the mean of the sum of independent variables equals the sum of the means, so the average pattern will be

$$f^2 = f_0^2 + \frac{\sigma^2}{D_0} \ , \tag{2.11}$$

where D_0 is the error free directivity, D is the directivity generated with the errors associated with, and $\sigma^2 = \sigma_{amp}^2 + \sigma_\phi^2$. Directivity normalized to D_0 is represented as

$$\frac{D}{D_0} \simeq e^{-\sigma^2} \simeq \frac{1}{1 + \sigma^2} \ . \tag{2.12}$$

Clearly it is notable that the side-lobe increase affects low side-lobe designs (e.g. ¡ -30 dBc) more adversely than the uniform amplitude -13 dBc side-lobes. The mean side-lobe level SLL is related to the design side-lobe level

SLL_d by

$$SLL = SLL_d \sqrt{\frac{1+\sigma^2}{D_0 \cdot SLL_d^2}} \ . \tag{2.13}$$

2.1.2.2 Directivity

Due to the random errors generated by various mechanisms, a phased array antenna's directivity occurs. This reduction is quantified by Skolink in [35] for omnidirectional element as

$$\frac{D}{D_0} = \frac{1}{1+\sigma_{amp}^2+\sigma_\phi^2} \ . \tag{2.14}$$

It is noticeable that the reduction in the directivity is not a function of array size; instead, it is only dependent on the error variance. It is noteworthy to state that reduced directivity is not a significant concern from a calibration standpoint for most arrays since the side-lobe distortion becomes a significant problem before directivity is reduced significantly.

2.1.2.3 Beam Pointing Errors

The beam pointing variance for a linear, symmetric, and equally spaced array at boresight is defined by [36–38], under the assumption that there is no element position and orientation error, as

$$\sigma_\theta^2 = \frac{\sigma^2 \sum_{\frac{-N}{2}}^{\frac{N}{2}} A_n^2 k^2 d^2 n^2}{\left[\sum_{\frac{-N}{2}}^{\frac{N}{2}} A_n^2 k^2 d^2 n^2\right]^2} \ , \tag{2.15}$$

and if the array has a uniform excitation then the beam pointing variance becomes

$$\sigma_\theta = \frac{3\sigma^2\lambda^2}{\pi^2 N^3 d^2} \ . \tag{2.16}$$

It is evident that larger arrays will have smaller beam pointing errors since their beamwidth is also smaller. The uniform linear array with d element spacing has a beamwidth of $\frac{0.886\lambda}{Nd}$, we can get the standard deviation of beam pointing error normalized to the 3 dB beamwidth as

$$\frac{\sigma_\theta}{\theta_3} = \frac{\sqrt{3}\sigma}{0.886\pi\sqrt{N}} = \frac{0.622\sigma}{\sqrt{N}} \ . \tag{2.17}$$

Generally speaking, the beam pointing errors are not significantly detrimental to the overall antenna pattern, and for a uniform linear phased array, they decrease slowly with the number of elements.

2.2 Array Calibration Terminology and Procedures

All active phased array antennas need to be calibrated in order to perform within their typical specifications such as side-lobe level, gain of the main beam, etc. These specifications can be translated into allowable amplitude and phase errors at the element level.

Depending on its statistical property, phase error may have a significant impact on the antenna beam pattern. If the error distribution remains uniform around the array, the nulls will be severely affected by losing 10 dB to 20 dB. If the phase error distribution is systematic, then the main beam will steer in a different direction. Phase error can be generated from various sources, including but not limited to the RF feed network, thermal effects in power amplifiers and low noise amplifiers, and group delay variations in filters. According to the international telecommunication provider (ITU) advanced antenna system (AAS), the recommended amplitude and phase error tolerance is $\pm 5^\circ$ and

± 0.5 dB, respectively, but this of course changes for different applications.

While there is a wide variety of calibration procedures available depending on a different system, practically all of them have the same goal to align each element's amplitude and phase correctly to achieve the system specification. Calibration can be divided into two broad categories according to [39, 40]. These are factory/initial calibration and in-situ calibration.

2.2.1 Initial Calibration

Initial calibration is usually conducted right after the antenna is manufactured. This is typically performed rigorously within different frequencies and temperatures. Though the process may include different equalization techniques (including nonlinear equalization [29, 40]) to tackle different hardware issues, this dissertation will be focused on overall element level amplitude and phase alignment. Often one needs to use equipment to calibrate arrays that are not intended to be fielded with the array; such a process is designated here as being external calibration. Internal calibration refers to the calibration scheme where the array itself can perform the calibration procedure. Sometimes there is dedicated equipment or elements fielded with the array, which can perform calibration. We will discuss more rigorously both options below.

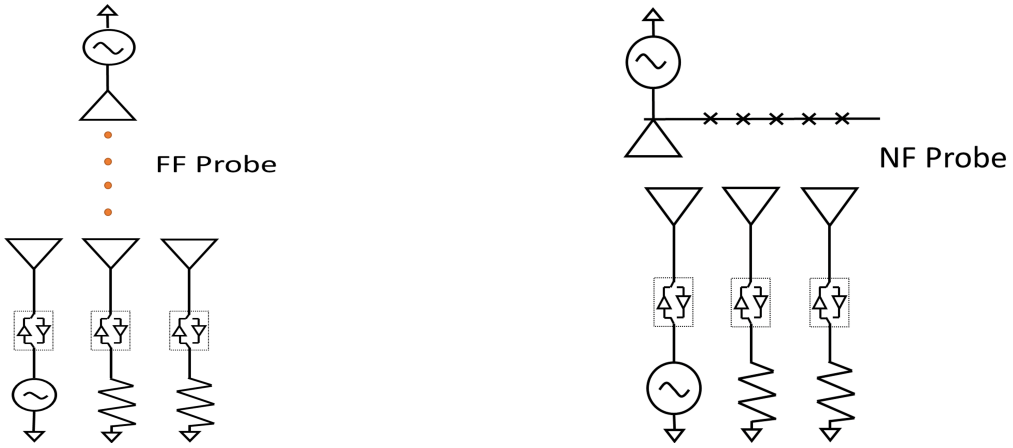

(a) External: Far-field (b) External: Near-field

Figure 2.2: External calibration using equipment that will not be fielded with the system

2.2.1.1 External Calibration

External calibration is usually performed in different antenna ranges such as near-field (NF) [9, 41–46] as depicted in Figure 2.2b, or far-field (FF) [47–51], as in Figure 2.2a. NF calibration is a widely accepted technique among researchers and is considered to be an accurate and mature process, with an typical accuracy limit on the order of 0.1 dB and 0.1° [40] in lower microwave frequencies. A voltage pattern is measured with a well-characterized probe within the near-field of the array. Typically the near-field probe is placed a little more than three-wavelength distance from the array. After probe compensation, the plane wave spectrum is derived from the captured voltage pattern, and fields are calculated from the plane wave spectrum. Since fields are known in terms of the plane wave spectrum, it is possible to observe element-level field variation using a "back projection" algorithm.

The most popular calibration method is the park and probe technique, where an NF scanner scans the array geometry to test all elements one by one.

This process typically needs to repeat for each element, each frequency within the bandwidth, for each phase state, and for each amplitude state to characterize the whole array [9]. The purpose of this calibration is to use transmittance S_{21} measurements to investigate the proper setting for attenuators and phase shifters [44] to meet the beam specification. Indeed this is a useful, widely accepted, powerful tool for array calibration. However, one should note that full calibration of an active array is highly measurement intensive. Depending on the system, thousands of measurements may be required to characterize the performance of each element fully. There is some calibration procedure reported using far-field measurement using FF calibration towers. Hezewijk [47] used an element excitation method where he measured the FF pattern by changing each element's excitation one by one under the assumptions of no mutual coupling and that the amplitude of the element under test was independent of the phase setting of the element. In [48], Aumann et al. showed an adaptive calibration technique using adaptive nulling. This technique can determine the amplitude and phase of the array element directly from far-field measurements using indirect (adaptive) processing of measurements. Hu, [49] proposed another novel method phase-match method (PMM), using far-field measurement to aligned a phased array without any expensive and complicated instrument. However, this arrangement requires a large far-field range. Another example by Fulton et al. [50] makes use of far-field measurements using a horn antenna without an anechoic chamber for a cylindrical array, and, using an alternating projection algorithm, they were able to align the amplitude and phase of CPPAR demonstrator while optimizing beamforming on this conformal surface.

Mano and Katagi in [52] proposed another method, rotation of the elec-

tric vector (REV), where they measured the composite field amplitude due to variation of the element phase shift to identify element level amplitude and phase. It utilizes the power only measurement while rotating the phase shifter of the element to extract the complex excitation. However, these measurements are strongly susceptible to excitation errors. Takahashi in [53] has a rigorous probabilistic analysis on excitation errors using the REV method. It is worth mentioning that one needs to continue the measurement process until it converges to a good beam pattern, which can be very cumbersome. Finally, in [54], they came up with a model that was capable of detecting the complex excitation of each element using power only measurements by making indirect estimates of these values through post-processing. Cases similar to REV are also found in [55–57].

Zheng introduced the mid-field calibration technique [58], shown in Figure 2.3c, where the transmitting signal was measured in three different positions, by a reference antenna, in front of the array for each element. While defining mid-field, the author argues that midfield would be considered such a distance where it is considered far-field for the element. Gu [59] theoretically analyzed the errors related to mid-field calibration and showed that given specific condition, the errors could be limited by 0.3 dB in amplitude and 5° of phase. Li also showed [60] another mid-field calibration technique where they asynchronously rotate one active element and keep the non-rotating elements in the on-off state.

2.2.1.2 Internal Calibration

The number of needed measurements is dramatically reduced in a digital array, as all elements can transmit and receive, irrespective of near- or far-field scan-

ning. The far-field pattern of each element can often be uniquely calculated for digital arrays. However, for active electronically scanned arrays, which have active and subarray digitized arrays with a limited number of beamformer outputs, it is possible to calculate the individual element pattern using techniques like control circuit encoding (CCE), depicted in Figure 2.3a, [61–63], unitary transform encoding (UTE) [62, 64], pseudo-noise gating (PNG) [65] and FFT based coding [66]. This measurement's primary objective is to minimize measurement number and time by keeping the probe parked in a specific place. Since the probe does not need to move within the plane, these techniques are getting popular. The basic concept is to make a sequence of measurements for N elements to form a vector, which can be defined as

$$V_m = \sum_{n=1}^{N} D_{mn} E_n \ , \tag{2.18}$$

where $m = 1 \cdot M \geq N$ or $V = \mathbf{C}E$ in matrix form. Here vector E has a length of M and is defined as the desired complex excitation of an individual element, which is a part of an overall sum of N signals. $C_{m,n}$ contains the encoding state of an array's elements, typically some orthogonal matrix or coefficients of an FFT. The desired values of the excitements are recovered by using,

$$E = D^{-1} V \ . \tag{2.19}$$

It is important to note that CCE uses toggling of individual bits of the phase shifter states and is hence more suitable for analog beamformers. In contrast, the FFT-based coding considered an average over a large number of phase shifts, and is therefore unable to characterize individual bits. It is not recommended to use PNG or UTE coding technique to calibrate analog

beamformers since they tend to rely on 180° phase-shifting without utilizing all available bits. However, these can be a strong candidate for digital beamforming arrays as the digital domain has more degrees of freedom for calibration. Takahashi [67], and Usin [68] reported that UTE and PNG based calibration method suffers to produce accurate results due to failures of a particular state of phase shifters. This happened because of phase shifter failure to impose the orthogonality of D_{mn}, which leads to an erroneous result. However, digital phased arrays are free from these errors due to their architecture.

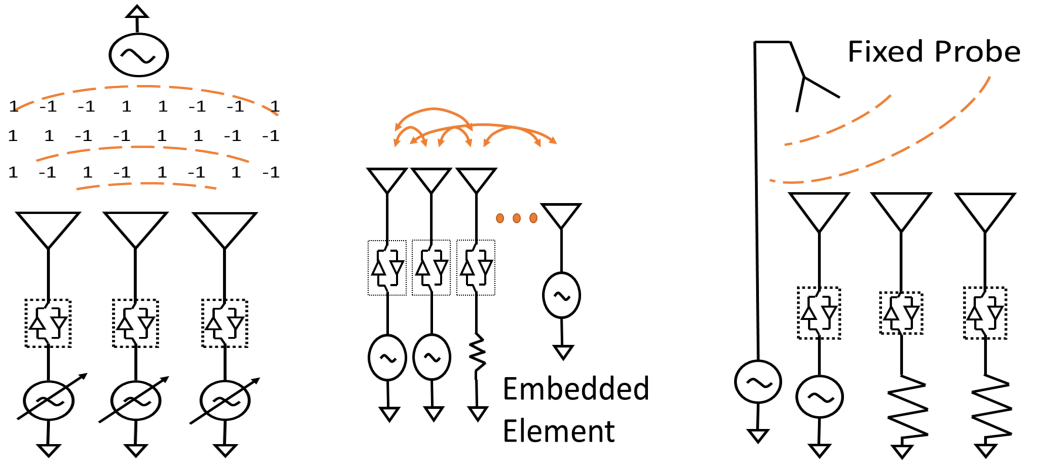

(a) Internal: code based

(b) Internal: mutual coupling

(c) Internal: fixed probe

Figure 2.3: Internal calibration using technique/equipment which will be fielded with the system

A mutual coupling based approach, shown in Figure 2.3b, proposed by Beker [69], was divided into two different calculations. An offline calculation can be done on any platform, and an online calculation carried out each time one wishes to calibrate the array. They first made a set, a collection of the equal geometric spacing element, assuming that they have the same inter-element coupling. For example, the couplings between all elements and their

neighbors one row directly above or below make up the $[1, 0]$ coupling set of a rectangular array, where $[1, 0]$ indicates the set's normalized row and column distance. This can be written in the form of the equation as

$$\left[\frac{D_{row}}{\Delta_{row}}, \frac{D_{col}}{\Delta_{col}}\right] = [q, p] \ , \tag{2.20}$$

where $0 \leq q \leq N_{row} - 1$ and $0 \leq p \leq N_{col} - 1$. D_{row} and D_{col} represent the dimensional row and column distance respectively, and Δ_{row} and Δ_{row} represent the column and row spacing. However, the offline calculation becomes rigorous for a minimum number of the equations to be solved. A minimum number of the linearly independent equations for a N element array is subjective. It depends on how the sets were defined. The most straight forward is to know the transmit and receive channel gain; for each channel, at least $2N$ linearly independent equations are needed to be solved. For example, let us consider a $N \times N$ array. Now for a set $[0, 1]$, as the nearest neighbor coupling in a row, the total number of pairs is $2N(N - 1)$. Here two elements create a pair, so in a specific row, there will be $N - 1$ pairs, and that is applicable for all N rows. Since both transmit and receive excitation is required for each element, the number of different measurements needed is twice the number of elements. Considering all the pairs, the number of equations will be the combination of those pairs. Since for transmit and receive two pairs are needed, the total number of equation will be the combination of them as ${}^{2N(N-1)}\mathbf{C}_2$. This is the total number of equations needed for the set $[0, 1]$. Obviously, for the different sets like $[0, 2]$, $[1, 2]$, a different number of equations are needed. For a good comparison, Table 2.2 is provided which is taken from [69] for a specific 8×8 array.

Reducing the number of equations is possible if a constraint on the distance

Set	General Formula	Number of pairs	Number of equation
$[0,1]$	$2N(N-1)$	112	${}^{112}\mathbf{C}_2 = 6216$
$[0,2]$	$2N(N-2)$	96	${}^{96}\mathbf{C}_2 = 4560$
$[1,0]$	$2N(N-1)$	112	${}^{112}\mathbf{C}_2 = 6216$
$[1,1]$	$4(N-1)^2$	196	${}^{196}\mathbf{C}_2 = 19110$
$[1,2]$	$4(N-2)(N-1)$	168	${}^{168}\mathbf{C}_2 = 14028$
$[0,2]$	$2N(N-2)$	96	${}^{96}\mathbf{C}_2 = 4560$

Table 2.2: Number of Equation Required for Five Sets of Pairs of Element for 8×8 Array

D is imposed. Since the mutual coupling effect is more recognizable in the adjacent or neighbor elements, a limit can be assumed judicially. He proposed another novel method [70], by taking two power-only measurements for each element. The first power measurement was taken by shifting the elements phase by $\frac{pi}{2}$, and the second one taken by turning off the element under test. It is yet another example of determining individual element responses through indirect measurements.

2.2.2 In-situ Calibration

Once the phased array is stationed, frequent in-situ calibration must be performed to maintain the antenna's performance within specification. Phased array antenna performance is sensitive to secondary parameters such as temperature change, component aging, and material degradation. So an in-situ calibration is necessary to maintain antenna beam shape as desired. Using additional equipment to ensure in-situ calibration is not very popular. These days engineers try to make a low-cost phased array, which is more sensitive to

the secondary parameters mentioned above over systems based on traditional, hermetically-sealed, and temperature compensated T/R modules. So in-situ calibration has a vital role in maintaining the specification and standards of the phased array. The in-situ calibration procedure can be subdivided into two categories. One is an introduction of specialized hardware on board with the array, and the other is using mutual coupling between elements.

2.2.2.1 Mutual Coupling

Mutual Coupling (MC) based calibration procedures eliminate the requirement of specialized hardware on board; instead, the elements can act themselves as a probe. Aumann first proposed this approach in [71]. Under certain assumptions discussed earlier, the mutual coupling between two adjacent elements is invariant to their position due to the periodicity of the array. This is true for both transmitting and receiving in many cases. Using this relationship in a pairwise comparison, Aumann showed that it is possible to calibrate the full array and predict the array pattern. Herd [72] showed the calibration procedure in a 32 element digital beamforming array by utilizing a closed-loop feed network. He enforced the equality of the average measured coupling from opposite traveling sources to calibrate the array. The advantage of using a full digital beamformer is the flexibility to measure individual element level coupling. Shnitkin [66] used a similar technique by injecting RF into the antenna through the coupler and calculating the phase corrections by taking the Fast Fourier Transform (FFT) of the measured excitation at the antenna terminal.

In general, coupling measurement is done by sending a signal from one element and receiving it in another. In the analog array domain, it is necessary to have two different beamformers, transmit and receive, to enable the MC

measurement. Two separate transceiver chains are also needed to emit a known waveform. In contrast, MC became suitable for digital arrays because of their unique ability to transmit and receive at the element level. It became more attractive as signals are generated and digitized at the element level. There is no coupling between transmit and receive analog beamformers – sometimes a MC calibration significant error source – in digital arrays.

The fundamental problem of using MC based calibration is the strong coupling between adjacent elements. Typically the coupling of -10 to -25 dB s found between adjacent elements, which can be very destructive for adjacent receivers as they can saturate the LNA. There is limited technology that can deal with the dynamic range requirements of regular receiver operation and process this large signal linearly. Agrawal provided a solution to deal with this problem in [73]. He used some sparsely populated internal array elements as passive calibration elements. These are roughly 1% of the total elements, did not have any T/R modules behind them, and did not share any active beamformer.

It should be noted that these initial calibration examples were done using a NF or FF chamber. This procedure applies to in-situ monitoring only. The coupling between the elements was reported to be on the order of -50 to -70 dB. Suppose a 20W transmitter was used, then the coupling would be in the -27 to -7 dBm range, which is manageable for some receiving elements. The dedicated calibration elements have a flexible dynamic range requirement since they are solely placed for calibration purposes. One major drawback of this proposed system is that the dedicated calibration elements needed to be calibrated frequently to maintain the calibration standard. Also, without the presence of an anechoic chamber or any external equipment, this small

coupling is prone to erroneous calculation due to small changes such radome reflections, any closely moving object, or strong wind [74]. An attractive solution was offered by Fulton [40], where he proposed a unique way to utilize the potential advantage of a digital array's capability of measuring the coupling to multiple elements directly from a high-power transmitting element source. He demonstrated that using attenuators in the RF path of the transceivers and separating the relative transmit and receive calibration process, it was possible to operate the array in full transmit power and full receive gain while using the coupling of adjacent elements without any significant distortion to receivers. This also diminishes the radome and wind effects, as the adjacent element coupling is strong enough to distinguish between actual and error signals.

2.2.2.2 Encoded In-Situ Calibration

Airborne radar and satellite communication systems tend to rely on a self-calibration approaches for in-situ calibration. The class of dedicated internal calibration hardware proposed by Shnitkin and Herd has become popular because of multiple advantages. First, the coupling mechanisms themselves are not radiative, which limits the concern regarding radome reflection. If the large array approximation is being used, an automatic array alignment is possible because of a high degree of matching in a corporate-fed calibration network. The corporate fed calibration network is a great choice to implement CCE, UTE, and PNG type code-based algorithms. Lee [75] used a low-cost, easy implementation technique where a transmission line signal injector, together with a phase toggling technique, was used to detect the signals. Hampson [76] introduced a "Multi-Element Phase-toggle" (MEP) method, which allows a simultaneous subgroup of element calibration using phase toggling along with

the FFT technique. The TerraSAR-X [65] was a German SAR satellite system that used a PNG coding technique and an additional calibration port in each TRM to monitor the in-situ calibration in space. They used a Hadamard encoding method and reported an element level calibration errors of 0.3 dB and 2.6°. The Uninhabited Airborne Vehicle Synthetic Aperture Radar (UAVSAR) AESA developed by JPL [43] was built to fly over 60,000 ft. altitude, so they developed a temperature-dependent calibration lookup table in the NF range and used this to monitor calibration standards using a dedicated calibration beamformer in the panel architecture. It was also demonstrated that coupled injection in front of the LNA can be used to receive calibration signals by [77, 78].

2.3 Chapter Summary

This chapter has mainly focused on the fundamentals of phased array antennas and has provided an exhaustive literature review on phased array calibration. It started with an overview of the pattern synthesis of phased array antennas for the typical linear and planar shape geometry. This section also indicates the impact of element excitation on the beam direction and side-lobe levels. Some important antenna parameters such as directivity, gain, and realized gains are also discussed. From the antenna measurement point of view, the far-field approximation is vital since this is a tool to measure the maximum allowable error in phase to consider it as far-field.

Next, a theoretical derivation of excitation errors is provided. A list of typical error sources for phased array antennas has been provided. Excitation errors can affect side-lobe, beam pointing, and directivity. An analytical approach is provided for quantifying these errors. Some of those errors in-

volved manufacturing or systematic error, and some are random. To address systematic and random errors, the array needs to be calibrated right after production. However, random errors can occur all the time and impact antenna performance; in-situ calibration techniques are used to address these random error related problems.

Finally, a literature review of existing calibration techniques has been provided, including initial and in-situ calibration, so that the reader can get an idea of challenges and opportunities in this field. Initial calibration is divided into two categories depending on which scheme is chosen. If it requires tools that will not be fielded during the antenna operation, it is named external calibration. In contrast, if the antenna is capable of calibration using onboard tools, it is defined as internal calibration. On the other hand, for in-situ calibration, the procedure is divided between using a mutual coupling method and some other fast algorithm. All the available methods are briefly described with proper citation. In the next chapter, a novel calibration technique will be introduced and modeled with the goal of fast calibration.

Chapter 3

Novel Fast Calibration of Phased Array

In the previous chapter, some of the phased array characteristics have been discussed. It was also established through an exhaustive literature review that, to maintain the specification (Beamwidth, SLL level) of the array, it has to be calibrated initially and monitored frequently once fielded. It was also clarified that there is no general calibration procedure that fits all the system. Calibration procedure varies widely within the different phased array systems due to different needs and available options. One common problem was repeatedly seen: irrespective of the calibration procedure, almost all of them required an expensive anechoic chamber, some testing equipment, and a great deal of time. For example, it is reported in [9] for THAAD radar, they near-field scanned each of 25344 T/R module individually for three times in receiving stage and two times for transmitting stage.

Active electronically scanned array renders a few attractive features towards the satellite antenna. AESA payload offers a re-configurable and flexible beam shape. With a processor, it can allow flexibility towards frequency to beam allocation [79] and power per beam for multiple beam steering capacity simultaneously. One major challenge of using AESA is the requirement of accurate control of the complex excitation (amplitude and phase) across the array aperture. This control ensures the critical quality of the key features like the beam to beam isolation, application for reusing frequencies, and beam pointing towards the coverage zone. There is a strong demand for a fast and efficient calibration procedure with minimal downtime in these applications. Since the system is subject to significantly impacting revenue generation capacity, it is the right candidate for implementing the fast calibration technique. The fast calibration technique is also critical for NF/FF range testing due to the reduced test time and cost associated with it. In this chapter, a novel fast calibration framework is proposed. The mathematical model and different techniques for analog and digital phased array system is discussed. Additionally, a robust error model has been developed.

3.1 Calibration Framework

The excitation coefficients for amplitude and phase needs to be accurately calibrated to generate beams with predictable antenna patterns. High RMS excitation errors are responsible for high side-lobes and beam pointing errors, limiting the system capability of reusing spatial frequency. This will also reduce the total bandwidth. The flexibility of active phased array antenna depends on how quickly and correctly it can determine the element level excitation coefficient to calibrate the array. This technology is applicable to any

system which has the flexibility to have a fixed probe in its quasi-near-field. For the validation purpose, a satellite user terminal for the ground segment is used in this dissertation.

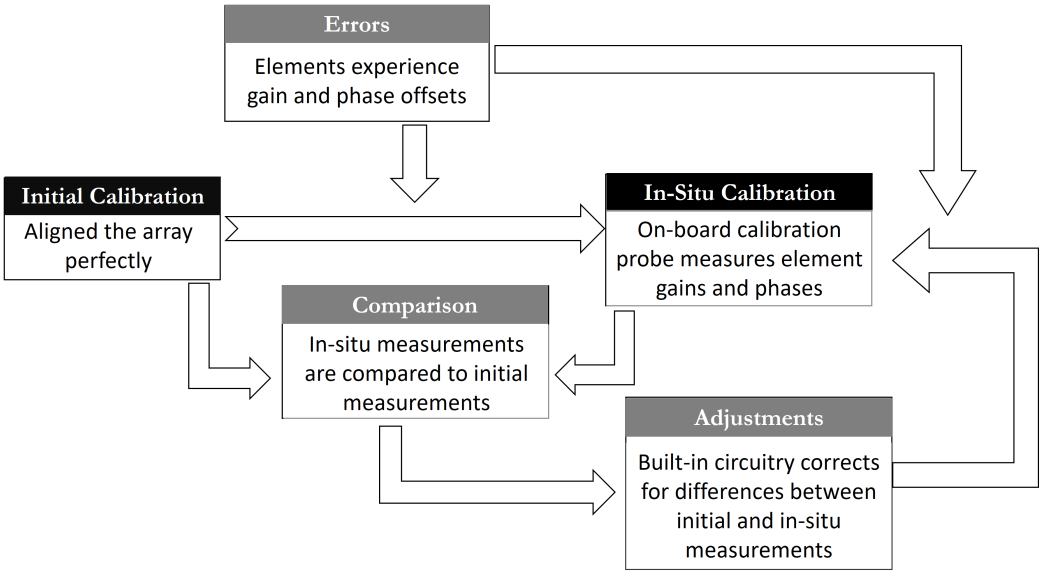

Figure 3.1: Basic block diagram of phased array antenna calibration procedure including initial and in-situ calibration with different error source and adjustment blocks

Some fast calibration techniques were mentioned in the previous literature, [58, 59, 80–83], all of them, irrespective of procedure, require expensive test equipment and test range for the calibration. A thorough search of the relevant literature on fixed probe in the quasi-near-field for calibration technique yielded no related article.

The typical block diagram of the calibration procedure is depicted in Figure 3.1. For the initial calibration, the proposed technique includes a fixed onboard probe in front of the array. A continuous-wave (CW) signal transmits from the calibration probe. The array's output is the summation of the received signal from all element paths of the beam under test. Then, by changing each element's phase and amplitude between the reference state and the

calibration state with orthogonal encoding, a sequence of RF signal is generated (TX mode) or received (RX mode) at the beam output port. After using the orthogonal encoding technique after down-conversion and A/D conversion, each element's relative phase and amplitude can be determined for the bit under calibration. Next, as the probe is sitting in the quasi-near-field, a probe compensation should be done since the wave in front of the antenna is a spherical wave in nature instead of a plane wave. This process should be repeated for all available bits for phase and amplitude under calibration. The steps mentioned above should also be repeated for all beams in different frequencies and temperature conditions to calibrate the entire beamformer initially.

After initial calibration, the array will be deployed for operation. The phased array also needs to be monitored while fielded as many primary and secondary parameters can affect the calibration with time. However, for in-situ calibration, it is not needed to calibrate the whole array. Instead, it is expected to be sufficient to recalibrate one phase and one amplitude bit and apply that calibration to all the other bits. This is based on the assumption that element-level excitation drifts are mostly caused by the active modules' thermal cycles and aging. While this proposed method is suitable for full digital airborne/satellite phased array systems, essentially, it can calibrate any sizable phased array, which requires this kind of fast calibration technique and has the option to fit in a fixed probe in the quasi-near-field for in-situ calibration.

3.2 Assumptions considered for this model

It is essential to describe what assumptions are taken into account for the phased array calibration method because if those assumptions are not satis-

fied, the whole process may fail to correct the complex weights at the element level. First, a linear relationship between a signal radiated from an element and that element's complex excitation control is considered. It is a moderately high accuracy assumption for digital arrays since phase shifting and attenuation is done digitally. Though there are unavoidable nonlinear characteristics at a high power level, this can be mitigated through proper power amplifier linearization. It is also assumed that all element patterns have the same shape to factor out the individual element pattern. This is known as "large array approximation" for phased arrays. Considering most of the element will be placed away from the corner of the array geometry, this assumption holds true for most of the phased array system. Additionally, it is assumed that there is no leakage between the transmitting and receiving channel for a full digital phased array because of their independent circuitry.

3.3 Quasi-Near-Field Approximation

The separation of space surrounding an antenna can be divided into three different regions, as shown in Figure 3.2. These are reactive near-field, radiating near-field, and far-field of the antenna. The mathematical formulation is derived by considering $\frac{\lambda}{2}$ dipole antenna as an array element. Getting a closed-form solution for a dipole antenna will be crucial for every point in the space, so some approximation has been made, especially for the far-field region, to simplify the formulation for a dipole antenna. Before going to the approximation, readers should have a clear picture of these different regions.

3.3.1 Reactive Near-Field

The reactive near-field is the space very close to the antenna. It is defined as

$$\text{reactive near-field: } 0 < r < 0.62\sqrt{\frac{D^3}{\lambda}}\ , \tag{3.1}$$

where D is the largest antenna dimension, r is the distance from the antenna, and λ is the wavelength. In this zone, the relationship between the strengths of **E**- and **H** -fields is critical to predict and measure as shown in Figure 3.2.

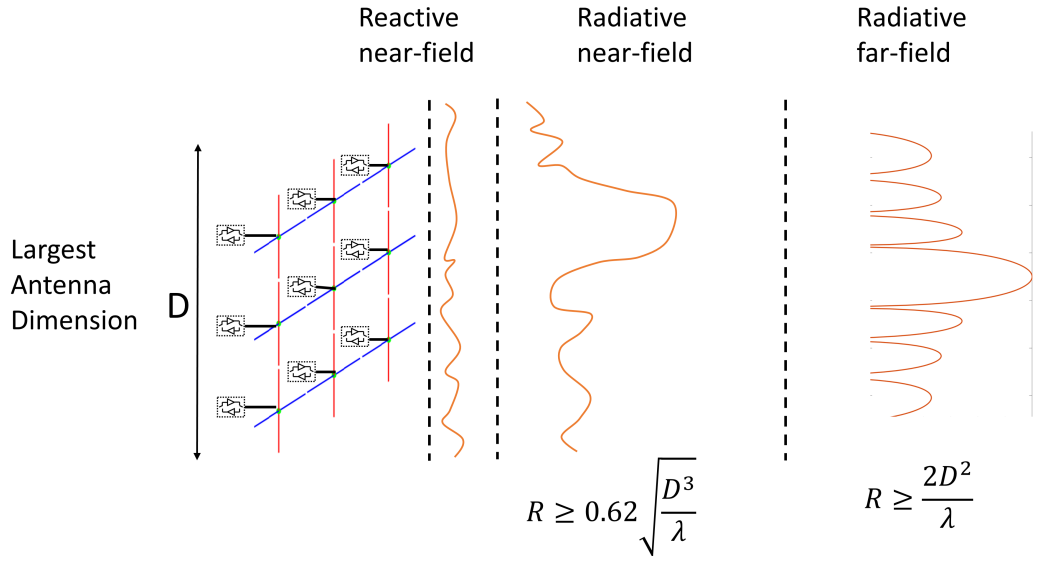

Figure 3.2: Nature of wave propagation in the reactive near-field, radiative near-field, and far-field respectively of a phased array antenna

Either field component can dominate within a very short distance, making the accurate power calculation challenging and resulting in erroneous measurements. This is because the phase difference between the fields needed to be calculated to measure power. In this region, the nature of the field is sensitive to EM absorption. Also, when measured, the reactive component of this region can provide ambiguous results. Usually, the power density is inversely

proportional to the square of the distance from the antenna, which does not hold in this region.

3.3.2 Radiative Near-Field

The radiative near-field region is also known as the Fresnel region because the field expressions are reduced to Fresnel integrals in this region. This is an intermediate region between reactive near-field and far-field. Mathematically this region can be defined as

$$\text{radiative near-field: } 0.62\sqrt{\frac{D^3}{\lambda}} \leq r < \frac{2D^2}{\lambda} \ , \tag{3.2}$$

where symbols hold their usual meaning. This region does not contain reactive field components as the distance is far enough that the reactive field components are highly evanescent. In this region, their field intensity has fallen enough to ignore them. Although radiant energy dominates this region, its mixture of magnetic and electric components is different from far-field.

3.3.3 Far-Field

This region comes after the radiative near-field region and mathematically defined as

$$\text{far-field: } \frac{2D^2}{\lambda} \leq r \leq \infty \ . \tag{3.3}$$

In this region, the electric and magnetic waves become the dominating field over the radiating fields. The antenna radiation pattern does not change; it is shaped with the change of distance r. The **E**- and **H**-fields become orthogonal, and the phase error became less than $\frac{\pi}{8}$ across the aperture. Antennas are used to send signals to a large distance wirelessly, which are considered as far-

field distances. According to [31], the ideal condition for measuring far-field radiation characteristics is the illumination of the test antenna by plane waves.

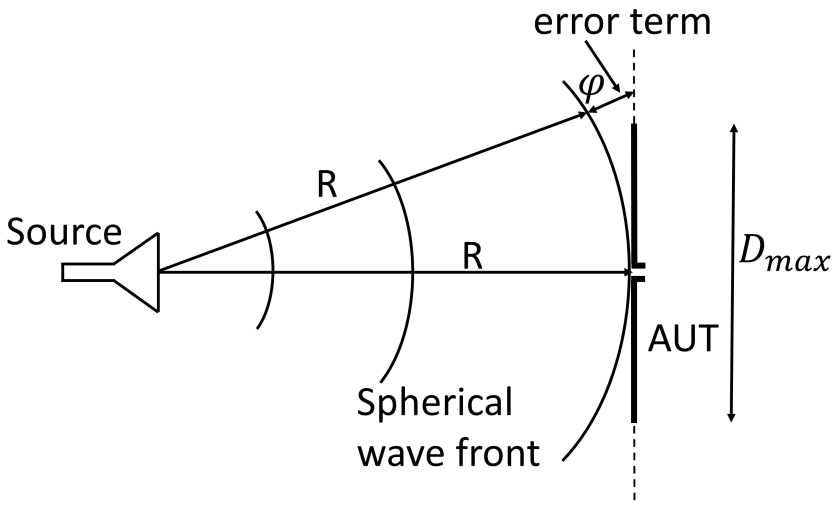

Figure 3.3: Phase error at the edge of a test antenna in far-field

However, in practice, the far-field generated by a probe is often approximated by a spherical wave-front. Although this ideal condition is not achievable, it can be approximated by separating the test antenna from the illumination source by a large distance on an outdoor range. As this separation distance increases, the curvature of the spherical phase front produced by the source antenna becomes more planar over the test antenna aperture. In this region, the radiation pattern does not change shape with distance (although the fields still die off as $\frac{1}{R}$, the power density dies off as $\frac{1}{R^2}$). This region is also dominated by radiated fields, with the E- and H-fields orthogonal to each other and the direction of propagation as with plane waves. If the maximum linear dimension of an antenna is D, then the following 3 conditions must all

be satisfied to be in the far-field region:

$$\begin{aligned} R &> \frac{2D^2}{\lambda} \\ R &>> D \\ R &>> \lambda \ . \end{aligned} \tag{3.4}$$

A graphical view of a far-field test is presented in Figure 3.3. However, the conditions, as mentioned above, are often altered for the phased array antenna. In a phased array antenna, using phase shifters, one can steer the beam by changing the phase of each element. In the far-field, also known as the Fraunhofer region, the maximum allowable phase error is given in [84] as

$$R_{min} = \frac{\pi}{4} \frac{D_{max}^2}{\varphi\lambda} \ , \tag{3.5}$$

where D_{max} is the maximum aperture dimension of the antenna, φ is the maximum allowable phase error, and λ is the wavelength of the wave. Now, consider a N element array with largest distance D_{max} and $\frac{\lambda}{2}$ spacing. It has an M bit phase shifter for changing the phase. So the maximum allowable phase error would be $\varphi = \frac{2\pi}{2^M}$. The maximum dimension can be defined as $D_{max} = (N-1)\frac{\lambda}{2}$. Since it is the finite array, an additional space of $\frac{\lambda}{4}$ is added in both the ends of the array. So the final maximum dimension will be $D_{max} = (N-1)\frac{\lambda}{2} + 2\frac{\lambda}{4} = N\frac{\lambda}{2}$. As per equation 3.5, this distance is the minimum, so the far-field must be equal or larger than that distance as shown in

$$\begin{aligned} \Rightarrow R_{min} &\geq \frac{\pi}{4} \frac{D_{max}^2}{\varphi\lambda} \\ \Rightarrow R_{min} &\geq 2^{M-5} N^2 \lambda \end{aligned} \ . \tag{3.6}$$

It is to be noted that the above approximation comes from the Taylor series expansion of the position vector given in [84]. More details can also be found in the paper written by Walter et al. [85].

3.3.4 Quasi-Near-Field

Since in our proposed model, the probe will be fixed with the antenna, it is not possible to be in the far-field region for practical reasons. Many pieces of literature tried to define far-field in different ways. Depending on the circumstance, there are different far-field boundary definition. Keiser mentioned in [86] that far-field is $\frac{\lambda}{2\pi}$ if $\frac{1}{r}$ term is dominant, $\frac{\lambda}{16}$ if the allowable error is less than 0.1 dB, $\frac{4D^2}{\lambda}$ for high accuracy antenna. Also [87] says the far-field boundary would be $\frac{3\lambda}{16}$ for dipoles, $\frac{2D^2}{\lambda}$ for antennas with $D \geq \lambda$. In case maximum dimension D being smaller than the wavelength, it is suggested in [88] to use an additional wavelength λ and count far-filed inner boundary as $\frac{2D^2}{\lambda} + \lambda$. In general, it is safe to say far-field starts form the region where the radial dependence of electric and magnetic field varies with $\frac{e^{jkr}}{r}$, where r is the radial distance from the antenna. The free space region from the antenna's surface to the far-field's starting point is considered the near-field region. As discussed earlier, it is divided into two regions reactive near-field and radiative near-field. The outer boundary of the reactive near-field region is $\frac{\lambda}{2\pi}$. However, from practical experience, it is suggested to take at least a wavelength distance or the outer boundary for reactive near-field. Beyond this distance, the EM field starts to propagate predominantly in phase, but they do not exhibit $\frac{e^{jkr}}{r}$ dependence until the inner boundary of the far-field reached. This is also known as Fresnel region and the boundary of this region is starting from $(\frac{D}{2\lambda})^{\frac{1}{3}}\frac{D}{2} + \lambda$ to the far-field region.

It is observed that radiative near-field is the right candidate for the proposed fixed probe placement, which is defined as quasi-near-field distance. Some of the mid-field external calibration schemes were reviewed in 2.2.1.1, where they proposed to consider the quasi-near-field in such a way that it must satisfy the individual element's far-field distance in terms of equation 3.4. After careful consideration, the distance of a fixed probe has been chosen as 10λ from the antenna to get an accurate result. For instance, 11.5 GHz operating frequency antenna, the probe should be placed at a minimum 0.26 meter distance.

3.4 Element Level Excitation Measurement

This research aims to accommodate the fast and efficient calibration technique for both analog and digital array. As discussed previously, in a digital array, every element can transmit and receive signals. This gives great flexibility to capture fields when transmitting from the probe in each element simultaneously. However, it is challenging to measure individual elements with analog beamforming architecture due to huge degradation in SNR. In ABF, the Wilkinson feed structure will look like a massive attenuator, which makes measuring the individual elements with good SNR almost impossible. In this section, the control circuit encoding technique is introduced, and a modified version of CCE is developed for efficient measurement of element level signal. The probe will be fixed in the proposed method, so there is no scanning to reduce the calibration measurement time.

3.4.1 Control Circuit Encoding

A better way to characterize the amplitude and phase of the array elements, called control circuit encoding, uses all elements during the calibration process. This technique first proposed by Silverstein [62], and later others worked on different applications as described in [80–83, 89, 90]. With this approach, the array elements all transmit (receive) simultaneously, but their phases are modulated according to the entries of a Hadamard matrix. Once the measurements are taken, this matrix is inverted to determine the amplitudes and phases.

To characterize the gains and phases of an N-element array, construct a Hadamard matrix of order M, where $M \geq N$. A Hadamard matrix is a square, invertible matrix whose entries are ± 1. A Hadamard matrix can be generated by the recursion

$$H_{2n} = \begin{bmatrix} H_n & H_n \\ H_n & -H_n \end{bmatrix} , \tag{3.7}$$

where

$$H_2 = \begin{bmatrix} 1 & 1 \\ 1 & -1 \end{bmatrix} . \tag{3.8}$$

During calibration, the array elements will be encoded according to the entries of this Hadamard matrix. A value of 1 in the matrix indicates that the element should transmit (receive) in its normal state, and a value of -1 indicates that the element should transmit (receive) in its encoded state. Encoding may be accomplished by attenuating the gain of an element or modulating its phase (in this case, the process is referred to as phase coding). Both encoding methods work, but using the phase shifters is desirable because, in this case, their performance can be determined during calibration.

Now, consider an $N \times N$ diagonal matrix d with the entries along the diagonal labeled $d(1), d(2), \cdots d(N)$. These entries correspond to the phase shift (or attenuation) applied to each element when it is in the encoded state. The calibration process uses pairs of measurements, with each measurement pair using two encoding rules, D^F and D^R. These rules are given by

$$D^F(m,n) \equiv \begin{cases} +1 & \text{for} \quad H(m,n) = 1 \\ d(n) & \text{for} \quad H(m,n) = -1 \end{cases} \tag{3.9}$$

$$D^F(m,n) \equiv \begin{cases} d(n) & \text{for} \quad H(m,n) = 1 \\ +1 & \text{for} \quad H(m,n) = -1 \end{cases} . \tag{3.10}$$

Here, D^F, forward encoding direction, and D^R, reverse encoding direction, refer to the command sent to element n at time m. At first glance, it may seem unintuitive why the encoding is applied in two different ways, but the difference between these matrices yields an important equality:

$$D^F(m,n) - D^R(m,n) = H(m,n)(1 - d(n)) \ . \tag{3.11}$$

The equation 3.11 shows that the difference between these two encoding methods yields a quantity proportional to the Hadamard matrix. Unlike the UTE method, CCE does not require any additional hardware as reported by [80]. The utility of this lies in that the equation may be solved even when the variable gain amplifier (VGA) and phase shifters are not an ideal component and subject to generate errors. The matrix form of this equality is given by $\boldsymbol{D^F - D^R = H_N(I - d)}$ where $\boldsymbol{I}$ is the identity matrix. Finally, the equation

can be solved to yield the matrix $\boldsymbol{I} - \boldsymbol{d}$ as

$$\boldsymbol{I} - \boldsymbol{d} = \boldsymbol{H_N^{-1}}(\boldsymbol{D^F} - \boldsymbol{D^R}) \ . \tag{3.12}$$

Here $\boldsymbol{I} - \boldsymbol{d}$ is a diagonal matrix that determines the actual values of $d(n)$. During calibration, this process may be done for multiple values of $d(n)$.

Let x_n be the signal obtained by element n without any phase shift applied, and let $\boldsymbol{X} = [x_1, x_2, \cdots x_n]^T$ be a column vector containing these values. The measurements taken during the calibration process are given by the following pair of vectors

$$\boldsymbol{Y}^F_{\mu 0} = [Y^F_{\mu 0}(1), Y^F_{\mu 0}(2), \cdots, Y^F_{\mu 0}(N)]^T \ , \tag{3.13}$$

$$\boldsymbol{Y}^R_{\mu 0} = [Y^R_{\mu 0}(1), Y^R_{\mu 0}(2), \cdots, Y^R_{\mu 0}(N)]^T \ , \tag{3.14}$$

where

$$y^F_{\mu 0}(m) = \sum_{n=1}^{N} \boldsymbol{D^F}(m,n) x_n \ , \tag{3.15}$$

$$y^R_{\mu 0}(m) = \sum_{n=1}^{N} \boldsymbol{D^R}(m,n) x_n \ . \tag{3.16}$$

Here, $\boldsymbol{Y}^F_{\mu 0}$ means that a measurement is to be taken using D^F for the encoding, μ is the encoding state that is to be switched in for encoded elements, and 0 means that only encoded elements should have this delay circuit switched in. The difference of these two vectors yields the important quantity

$$\boldsymbol{Y}^F_{\mu 0} - \boldsymbol{Y}^R_{\mu 0} = \boldsymbol{H_M}(\boldsymbol{I} - \boldsymbol{d})\boldsymbol{X} \ . \tag{3.17}$$

Now let

$$\begin{aligned} \boldsymbol{Z_{\mu 0}} &= \boldsymbol{H_M^{-1}}(\boldsymbol{Y_{\mu 0}^F} - \boldsymbol{Y_{\mu 0}^R}) \\ &= \boldsymbol{H_M^{-1}}(\boldsymbol{D_\mu^F} - \boldsymbol{D_\mu^R})\boldsymbol{X} \ , \\ &= (\boldsymbol{I} - \boldsymbol{d_\mu})\boldsymbol{X} \end{aligned} \tag{3.18}$$

where, $\boldsymbol{Z_{\mu 0}}$ contains the values of x_n, where each x_n has the delay circuit μ switched in. If the delay circuit μ are assumed to be ideal, then the values of $\boldsymbol{X}$ can be directly determined by dividing both sides by $(\boldsymbol{I} - \boldsymbol{d_\mu})$. However, this is not always the case, so it is desirable to determine the coefficients of $\boldsymbol{d_\mu}$. To accomplish this, another pair of measurements are taken using the same process as above, with one change. Denote this new pair of measurements as $\boldsymbol{Y_{\mu\nu}^F}$ and $\boldsymbol{Y_{\mu\nu}^R}$. In this case, the delay circuit ν is switched in for all elements, whether encoded or not. This new measurement is given by

$$\boldsymbol{Z_{\mu\nu}} = (\boldsymbol{I} - \boldsymbol{d_\mu})\boldsymbol{d_\nu}\boldsymbol{X} \ . \tag{3.19}$$

The values of $\boldsymbol{d_\nu}$ may be obtained by dividing $\boldsymbol{Z_{\mu\nu}}$ by $\boldsymbol{Z_{\mu 0}}$:

$$\frac{\boldsymbol{Z_{\mu\nu}}}{\boldsymbol{Z_{\mu 0}}} = \frac{(\boldsymbol{I} - \boldsymbol{d_\mu})\boldsymbol{d_\nu}\boldsymbol{X}}{(\boldsymbol{I} - \boldsymbol{d_\mu})\boldsymbol{X}} = \boldsymbol{d_\nu} \ . \tag{3.20}$$

It is noteworthy that $\boldsymbol{Z_{\mu 0}}$ and $\boldsymbol{Z_{\mu\nu}}$ are vectors, and this is element-wise division, not matrix division. Now, to uncover the values of $\boldsymbol{X}$ (which represent the amplitude and phase of each element), all that remains is to characterize $\boldsymbol{d_\mu}$ in the same way as in equation 3.20, and dividing $\boldsymbol{Z_{\mu 0}}$ by $\boldsymbol{I} - \boldsymbol{d_\mu}$:

$$\boldsymbol{X} = \frac{\boldsymbol{Z_{\mu 0}}}{\boldsymbol{I} - \boldsymbol{d_\mu}} \ . \tag{3.21}$$

It is implicit in the above derivation (and in [62]) that the phased array system to be calibrated uses delay circuits to shift the phase of the elements,

but this is not necessary: the elemental amplitudes and phases can be characterized with any form of phase modulation. Finally, note that not all phase settings need be characterized in order to calibrate the array. Generally, there are only three measurements that must be taken.

Encoding Phase	**Added Phase**	**Stored value**
ϕ_1	0	$\boldsymbol{Z_{\phi_1 0}}$
ϕ_2	0	$\boldsymbol{Z_{\phi_2 0}}$
ϕ_2	ϕ_1	$\boldsymbol{Z_{\phi_2 \phi_1}}$

Table 3.1: Minimum number of measurements necessary for calibrating a phased array antenna

Table 3.1 summarizes the bare-minimum calibration process. First, a phase shift of ϕ_1 is chosen for encoding. Then, it is necessary to determine the actual phases applied by ϕ_1. From equation 3.20, this is determined by taking the quotient of $\frac{\boldsymbol{Z_{\phi_2 \phi_1}}}{\boldsymbol{Z_{\phi_2 0}}}$. Once these effective phases are determined, $\boldsymbol{X}$ is found by dividing $\boldsymbol{Z_{\phi_1 0}}$ by $\boldsymbol{I - d_{\phi_1}}$ as in equation 3.21. At this point, it is important to note that calibration is effectively carried out by comparing the in-situ measurements $\boldsymbol{X^*}$ to measurements of the calibrated array $\boldsymbol{X}$. That is, there must be some standard set of values that the in-situ measurements will be compared.

3.4.2 Modified CCE

In Section 3.4.1, the CCE method was discussed briefly. Readers can already notice that this technique's success largely relies on the orthogonality of the coding scheme. Theoretically, one can encode the system in many different

ways as needed as long as the orthogonality has been maintained. Now, in modified CCE technique, Each elements complex excitation (amplitude and phase) is represented by $ae^{\frac{jn\pi}{4}}$. The unit circle of complex values is depicted in Figure 3.4. Assuming the availability of adequate phase resolution to get 180° phase shift from the reference phase, the modified CCE can provide better SNR over amplitude-based coding.

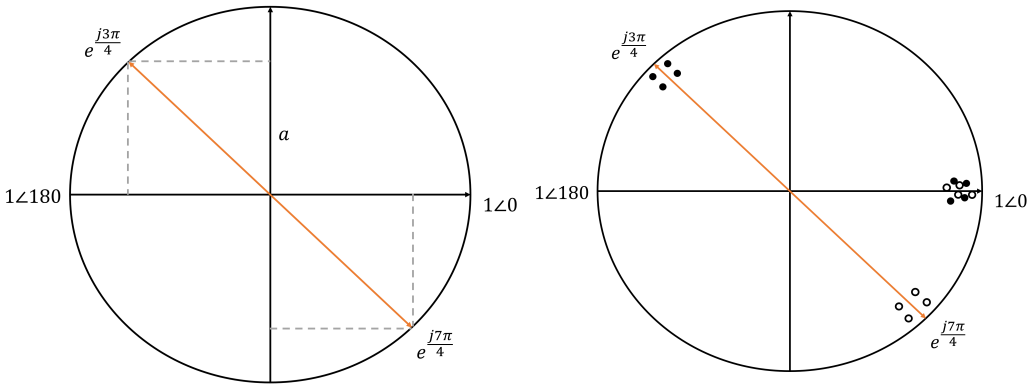

(a) Phase components in unit circle (b) Sample response measurement

Figure 3.4: Sample phase components and typical response for modified CCE

Consider an example of this modified technique. A four element array is examined for simplicity. Each received measurement is denoted as y_n. Each row of encoding matrix represents one measurement m_n. Total 12 measurements needed to be taken to extract the individual element response. The three measurements in terms of mathematical format can be represented as

$$M_1 = \begin{bmatrix} e^{\frac{j3\pi}{4}} & e^{\frac{j3\pi}{4}} & e^{\frac{j3\pi}{4}} & e^{\frac{j3\pi}{4}} \\ e^{\frac{j3\pi}{4}} & 1 & e^{\frac{j3\pi}{4}} & 1 \\ e^{\frac{j3\pi}{4}} & e^{\frac{j3\pi}{4}} & 1 & 1 \\ e^{\frac{j3\pi}{4}} & 1 & 1 & e^{\frac{j3\pi}{4}} \end{bmatrix} \begin{bmatrix} y_1 \\ y_2 \\ y_3 \\ y_4 \end{bmatrix} = \begin{bmatrix} m_1 \\ m_2 \\ m_3 \\ m_4 \end{bmatrix}, \tag{3.22}$$

$$M_2 = \begin{bmatrix} e^{\frac{j7\pi}{4}} & e^{\frac{j7\pi}{4}} & e^{\frac{j7\pi}{4}} & e^{\frac{j7\pi}{4}} \\ e^{\frac{j7\pi}{4}} & 1 & e^{\frac{j7\pi}{4}} & 1 \\ e^{\frac{j7\pi}{4}} & e^{\frac{j7\pi}{4}} & 1 & 1 \\ e^{\frac{j7\pi}{4}} & 1 & 1 & e^{\frac{j7\pi}{4}} \end{bmatrix} \begin{bmatrix} y_1 \\ y_2 \\ y_3 \\ y_4 \end{bmatrix} = \begin{bmatrix} m_5 \\ m_6 \\ m_7 \\ m_8 \end{bmatrix} , \tag{3.23}$$

$$M_3 = \begin{bmatrix} 1 & 1 & 1 & 1 \\ 1 & 1 & 1 & 1 \\ 1 & 1 & 1 & 1 \\ 1 & 1 & 1 & 1 \end{bmatrix} \begin{bmatrix} y_1 \\ y_2 \\ y_3 \\ y_4 \end{bmatrix} = \begin{bmatrix} m_9 \\ m_{10} \\ m_{11} \\ m_{12} \end{bmatrix} . \tag{3.24}$$

As the measurements are already taken, all it left is to process the data. By adding M_1 and M_2 then subtract this from M_3 will generate,

$$M_3 - (M_1 + M_2) = \begin{bmatrix} 1 & 1 & 1 & 1 \\ 1 & -1 & 1 & -1 \\ 1 & 1 & -1 & -1 \\ 1 & -1 & -1 & 1 \end{bmatrix} \begin{bmatrix} y_1 \\ y_2 \\ y_3 \\ y_4 \end{bmatrix} = \begin{bmatrix} m_9 - m_1 - m_5 \\ m_{10} - m_2 - m_6 \\ m_{11} - m_3 - m_7 \\ m_{12} - m_4 - m_8 \end{bmatrix} . \tag{3.25}$$

One should observe that the encoding matrix became Hadamard matrix of order 4. The Hadamard matrix's unique characteristic is its inverse also gives as a scaled value of the same matrix. So it will be straightforward to extract the y_n from this point. This will be applicable for any reference phase with it's 180° phase shift to maintain the orthogonality.

Some of the analog phased array systems can excite individual elements using the RF chain. These types of arrays are commonly known as an active electronically scanned array. In that case, it is possible to use individual element level transmit or receive signal and then use the probe compensation to calibrate the array. In this way, it will be only N measurement needed to

calibrate the array. However, for a better SNR, one can take two measurement 180° apart and subtract them.

3.4.3 Mathematical Model

To analyze the performance of the CCE algorithm a mathematical framework was created and implemented in ®MATLAB to simulate the calibration of a phased array in the presence of several error parameters, including noise, leakage, probe displacement, and malfunctioning phase shifters.

3.4.3.1 General Array Model

Let A be a $m \times n$ planar array with a uniform spacing d between elements. The number of elements is calculated as $N = mn$. The Cartesian coordinates for an element are given by

$$r_e(i,j) = \begin{bmatrix} x(i,j) \\ y(i,j) \\ z(i,j) \end{bmatrix} = \begin{bmatrix} (j-1)*d \\ (i-1)*d \\ 0 \end{bmatrix}, \text{where } 1 \leq i \leq n, 1 \leq j \leq m \ , \quad (3.26)$$

that is, element $(1,1)$ lies at the origin and element (n,m) lies in the first quadrant of the $x-y$ plane. This convention has been chosen to reflect ®MATLAB's matrix indexing of row-then-column.

Let the nominal embedded element pattern be denoted $F_n(\theta,\phi)$, with each element terminating into a Z_0 load. Let G_n denote the gain of the LNA for the n^{th} element $H_n(A_n,\theta_n)$ denote the effective transfer function of the gain/phase adjustor for the n^{th} element. Here A_n is the voltage gain adjustment in dB, and θ_n is the phase adjustment in degrees. Now, let x_n be a voltage wave down into the LNA, and y_n be the corresponding voltage wave down into the

power combiners. Then y_n and x_n are related by

$$y_n = G_n H_n(A_n, \theta_n) x_n \ , \tag{3.27}$$

it can be represented in matrix form as

$$\boldsymbol{Y} = \boldsymbol{GHX} \ , \tag{3.28}$$

where $\boldsymbol{Y} = [y_1, y_2, \cdots, y_n]$. If the voltage wave of post-LNA is defined as $x_n^{'}$, then $y_n = H_n(A_n, \theta_n) x_n^{'}$. This suggests that gain and phase correction is accomplished by passing the appropriate values of A_n and θ_n into the system H_n for each element. After the LNA and phase shifters, each y_n is added together through the power combiners to produce the total received signal. Let P_n denote the transfer function from y_n to $\boldsymbol{Y}$. Ideally, $P_n = \frac{1}{\sqrt{N}}$, so $Y = \frac{1}{\sqrt{N}} \sum_{n=1}^{N} y_n$. Let the effective element pattern be denoted as

$$F_n^E(\theta, \phi, A_n, \phi_n) = F_n(\theta, \phi) G_n H_n(A_n, \phi_n) \ . \tag{3.29}$$

The array's overall pattern is given by the sum of each element pattern as

$$R^{Eff}(\theta, \phi, A_n, \phi_n) = \sum_{n=1}^{N} F_n^E(\theta, \phi, A_n, \phi_n) \ . \tag{3.30}$$

3.4.3.2 Radiation Model

In the far-field plane wave assumption is true, and phase calculation is progressive, as shown in Figure 3.5a. However, this is not the case for quasi-near-field probe since each angle is different as depicted in Figure 3.5b. So a radiation model is needed. The radiation model used throughout this chapter is quite

simple. No considerations are given for the effects of polarization or directionality. This means that the actualization of a calibration setup will be presented with more errors than appear in the simulations to follow.

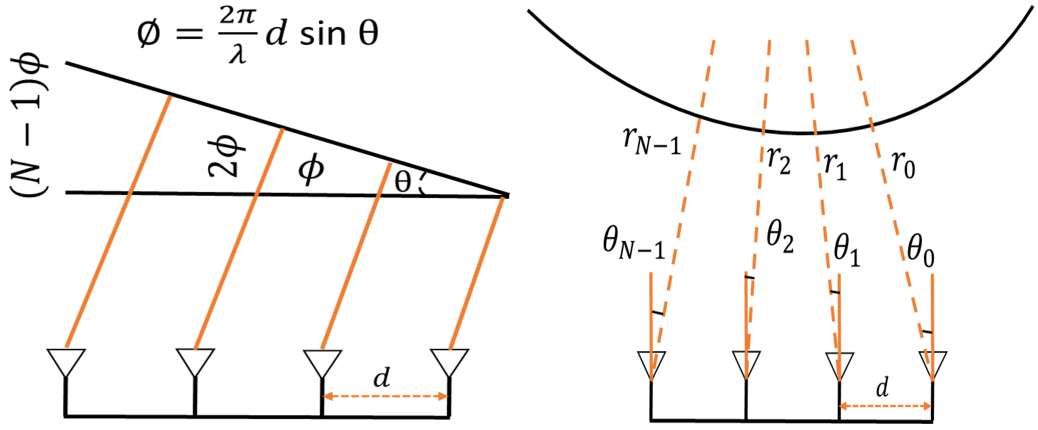

(a) Far-field plane wave (b) Quasi-near-field spherical wave

Figure 3.5: Different character of propagating wave in far-field and quasi-near-field

Since an isotropic antenna is being used, it is known that amplitude at any point in the space is determined based on the idea that the radiating energy must be constant for any spherical surface centered around the source. Therefore if a source and the receiver are separated by a distance r, and the operating frequency is f, then the field amplitude and phase [91], [92], may be given by

$$R(r, a, \lambda) = \frac{a}{r} \exp(-j2\pi \frac{r}{\lambda}) = \frac{a}{r} \exp(-j2\pi r \frac{c}{f}) \ , \tag{3.31}$$

where a is a scaling factor. If element n is separated from the calibration probe by a distance r_n, then it is assumed that the received signal is proportional to the electric field strength. Since only relative values matter for the calibration process, since it will be compared with the standard value, it will be assumed that the received signal is equivalent to the function R. If element n is sepa-

rated from the calibration probe by a distance r_n, then it is assumed that the received signal x_n is proportional to the electric field strength and the received signal x_n is equivalent to the function $R(r_n, a, \lambda)$.

3.4.3.3 Leakage

A prevalent form of error in an array is called leakage. In any electrical system, time-varying electric fields through one pathway can induce a small current in another, and this is how leakage works. The effect of leakage is simple: part of the signal acquired by one element will be seen by some of the other elements in the array. Thus, it is not sufficient to assume that each element has perfectly isolated electrical pathways. As a result, each y_n will be a function of x_m, for $1 \leq m \leq N$. Below is a diagram of a two-element phased array, with four leakage parameters shown in Figure 3.6.

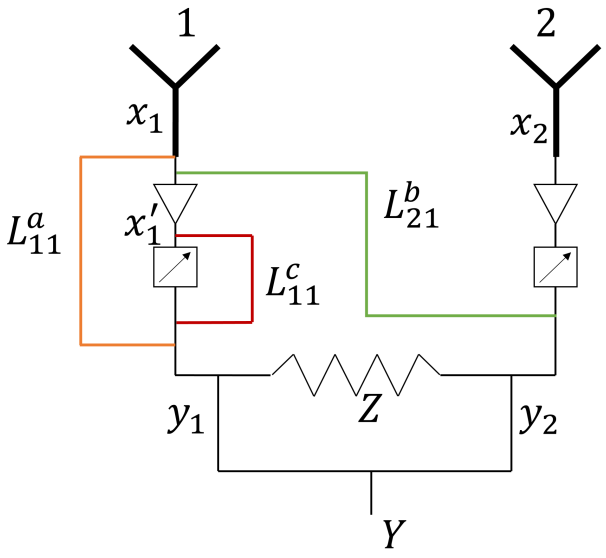

Figure 3.6: Four different leakages for two adjacent elements

In an ideal array, the signal acquired by the element 1 will be amplified by an LNA, have its phase and gain adjusted, and then added to the signal acquired by the element 2 through the power combiners. However, portions of the signal at each node may appear at other nodes in the array. Here, there are four leakage parameters: L^a, L^b, L^c, and L^d. Here, L^d_n refers to the total leakage from all elements x_m into x_n.

Let $L^a_{n,m}$, denote the leakage from x_m to y_n. When the array is receiving, the net effect of this leakage parameter, as seen from Z, is given by

$$L^a_{total} = \sum_{n=1}^{N}\sum_{m=1}^{N} x_n L^a_{n,m} P_n = \frac{1}{\sqrt{N}}\sum_{n=1}^{N}\sum_{m=1}^{N} x_n L^a_{n,m} \ . \tag{3.32}$$

In ®MATLAB, all leakage terms were represented in matrix form as shown

$$\boldsymbol{L^a} = \begin{pmatrix} L^a_{11} & \cdots & L^a_{1,N} \\ \vdots & \ddots & \vdots \\ L^a_{N,1} & \cdots & L^a_{N,N} \end{pmatrix} \ . \tag{3.33}$$

Let $L^b_{n,m}$ denote the leakage from x_m to $x^{'}_n$. The total effect of this leakage term is given by

$$\begin{aligned} L^b_{total} &= \sum_{n=1}^{N}\sum_{m=1}^{N} x_n L^b_{n,m} H_n(A_n,\theta_n) P_n \\ &= \frac{1}{\sqrt{N}}\sum_{n=1}^{N}\sum_{m=1}^{N} x_n L^b_{n,m} H_n(A_n,\theta_n) \end{aligned} \ , \tag{3.34}$$

this means that the leakage term L^b has different effects depending on the value of H_n. Let $L^c_{n,m}$ denote the leakage from $x^{'}_m$ to y_n. Again, the net effect

of this leakage term is given by

$$\begin{aligned} L^c_{total} &= \sum_{n=1}^{N}\sum_{m=1}^{N} x_n L^c_{n,m} G_n P_n \\ &= \frac{1}{\sqrt{N}} \sum_{n=1}^{N}\sum_{m=1}^{N} x_n L^c_{n,m} G_n \end{aligned} \quad . \tag{3.35}$$

One can expect the leakage term L^c to have the most significant effect, as the LNA amplifies it in each element. Now, let a column vector x_N represent the voltage waves down into the LNA for each element. The total matrix representation of the array on receive is given by

$$\boldsymbol{Y} = (\boldsymbol{GH} + \boldsymbol{L^a} + \boldsymbol{GL^c} + \boldsymbol{HL^b})\boldsymbol{X} \ , \tag{3.36}$$

note that this is a natural extension of the ideal situation where $Y = GHX$

3.5 Chapter Summary

In this chapter, the mathematical framework of the proposed calibration method has been laid out. The probe distance at quasi-near-field is explained and a radiation model is proposed. Element level excitation measurement is explained for the analog phased array with the use of orthogonal matrix-based measurement. Two different techniques are discussed briefly. This process can be ignored for a full digital array as it can transmit and receive at the element level. However, the rest of the framework is equally applicable to both digital and analog arrays. The leakage model has also been developed to tackle unavoidable error sources. Since the fundamental theory has been described in this chapter, a simulation of the whole system will be demonstrated in the next chapter.

Chapter 4

Sand-Box Simulation to Analyze Phased Array Antenna Using Fixed probe

In this chapter, the proposed fixed probe-based one-shot calibration technique will be simulated using a ®Matlab sand-box. This toolbox is developed to analyze and simulate the calibration technique presented in Chapter 3. First, the whole system's S parameter is simulated to address the mutual coupling, edge element effect, and probe effect of the designed phased array. The mathematical framework has been developed and analyzed in ®MATLAB, to determine the "ground-truth" reference, probe response calculation for each element, and generating complex calibration weight to account for both amplitude and phase. The simulated phased array consists of ideal dipole elements probed by a second array of dipoles from a quasi-near-field locations. To begin with, a

classical induced electromotive force (EMF) method [31, 93] is used to calculate mutual impedance matrix Z for the whole system, which includes array-array, array-probe, and probe-probe (if an array of probe being used) configurations. Next, the S parameters from the mutual impedance matrix Z is calculated. Once the whole S parameters of the system are calculated, the coupling of the different combinations of the array element can be quantified. Then, the responses of outgoing waves, defined as b_n, from the incoming waves, defined as a_n, of array elements are calculated by assuming the ideal array behavior. After that, some of the sand-box characteristics are shown to analyze the array. Finally, a calibration procedure is simulated and compared with the "ground-truth" to analyze the calibration standard. Here it is assumed that the array is fully digital and capable of transmitting and receive signals in element levels. In the case of an analog array, the process of measuring individual element excitation has already discussed briefly in Section 3.4 using CCE and modified CCE methods. It noteworthy to mention that the results in this chapter is previously published in [94, 95].

4.1 Sand-Box Simulation Procedure

4.1.1 User Input

The sand-box is created so that users can choose the frequency of the system, element numbers, linear or planar array geometry, the dimension of the dipoles, spacing between two elements, probe distance, and probe position. Users can choose where they want the probe, be it in the center of the array or corner.

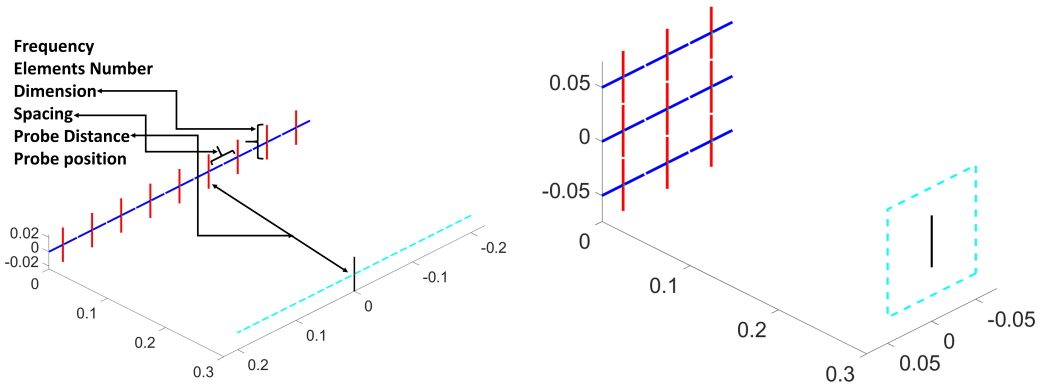

(a) Linear array of $\frac{\lambda}{2}$ dipole (b) Planar array of $\frac{\lambda}{2}$ dipole

Figure 4.1: Simulated linear 9 element and 3×3 planar array front end based on user inputs. From [94], ©IEEE

After getting input from the user, the sand-box creates the whole system geometry by positioning everything virtually. In the Figure 4.1(From [94], ©IEEE), two different arrangement is shown. In Figure 4.1a a 9 element linear array is populated with $\frac{\lambda}{2}$ dipole antenna with a single probe in front of the array at 3λ distance with an operating frequency of 3 GHz. Also, in Figure 4.1b, a 3×3 planar array is simulated with the same dipole and same frequency. The probe is positioned in the center of the array. The sand-box is capable of generating any configuration of arrays as specified by the user.

4.1.2 Self-Impedance Calculation

After getting the user input, the physical modeling of the array is already determined. Now the dipoles' self-impedance will be calculated to generate the diagonal component of the impedance matrix Z.

Based on the current distribution and tangential electric field along the surface of the wire, the induced potential developed at the terminals of the

dipole based on the maximum current is given by [96]

$$V_m = \int_{-\frac{l}{2}}^{\frac{l}{2}} dV_m = -\frac{1}{I_m} \int_{-\frac{l}{2}}^{\frac{l}{2}} I_z(\rho = a, z = z^{'}) E_z(\rho = a, z = z^{'}) dz^{'} \ , \tag{4.1}$$

where I_m is the maximum current, and V_m is the maximum voltage corresponding to the current. The input impedance with this maximum current is given by

$$Z_m = \frac{V_m}{I_m} = -\frac{1}{I_m^2} \int_{-\frac{l}{2}}^{\frac{l}{2}} I_z(\rho = a, z = z^{'}) E_z(\rho = a, z = z^{'}) dz^{'} \ , \tag{4.2}$$

for a wire dipole, the total current I_z is uniformly distributed around the surface of the wire, and it forms a linear current sheet J_z which is expressed as

$$I_z = 2\pi a J_z = I_m \sin[k(\frac{l}{2} - |z^{'}|)] \ , \tag{4.3}$$

therefore equation 4.2 can be written as

$$Z_m = -\frac{1}{I_m} \int_{-\frac{l}{2}}^{\frac{l}{2}} \sin[k(\frac{l}{2} - |z^{'}|)] E_z(\rho = a, z = z^{'}) dz^{'} \ . \tag{4.4}$$

After rigorous calculation, the final equations are given in [96], where the self-impedance can be expressed as

$$Z_{in} = R_{in} + jX_{in} \ , \tag{4.5}$$

and R_{in} and X_{in} can be obtained from the equations

$$\begin{aligned} R_{in} &= \frac{R_m}{\sin^2(\frac{kl}{2})} \\ X_{in} &= \frac{X_m}{\sin^2(\frac{kl}{2})} \end{aligned} \ . \tag{4.6}$$

Here R_r and X_m are given as

$$R_m = \frac{\eta}{2\pi}\Big\{C + \ln(kl) - C_i(kl) + \frac{1}{2}\sin(kl)[S_i(2kl) - 2S_i(kl)] + \frac{1}{2}\cos(kl)[C + \ln(\frac{kl}{2}) + C_i(2kl) - 2C_i(kl)]\Big\} \quad , \tag{4.7}$$

$$X_m = \frac{\eta}{4\pi}\Big\{2S_i(kl) + \cos(kl)[2S_i(kl) - S_i(2kl)] - \sin(kl)[2C_i(kl) - C_i(2kl) - C_i(\frac{2ka^2}{l})]\Big\} \ , \tag{4.8}$$

where $C = 0.5772$ is Euler's constant, $S_i(x)$ and $C_i(x)$ are the sine and cosine integrals defined as

$$\begin{aligned} S_i(x) &= \int_0^x \frac{\sin(\tau)}{\tau} d\tau \\ C_i(x) &= \int_\infty^x \frac{\cos(\tau)}{\tau} d\tau \\ C_{in}(x) &= \int_0^x \frac{1 - \cos(\tau)}{\tau} d\tau \end{aligned} \quad . \tag{4.9}$$

4.1.3 Mutual Impedance Calculation

The presence of an obstacle always alters the current distribution; hence, the field radiated, and in turn, the antenna's input impedance. Thus, the antenna performance depends not only on its own excitation but also on the excitation of the neighboring elements. The input impedance of the antenna in the presence of the other elements or obstacles depends upon the self-impedance and the mutual impedance between the driven element and the other obstacles or elements. Using the induced EMF method described in [96] the mutual impedance can be quantified.

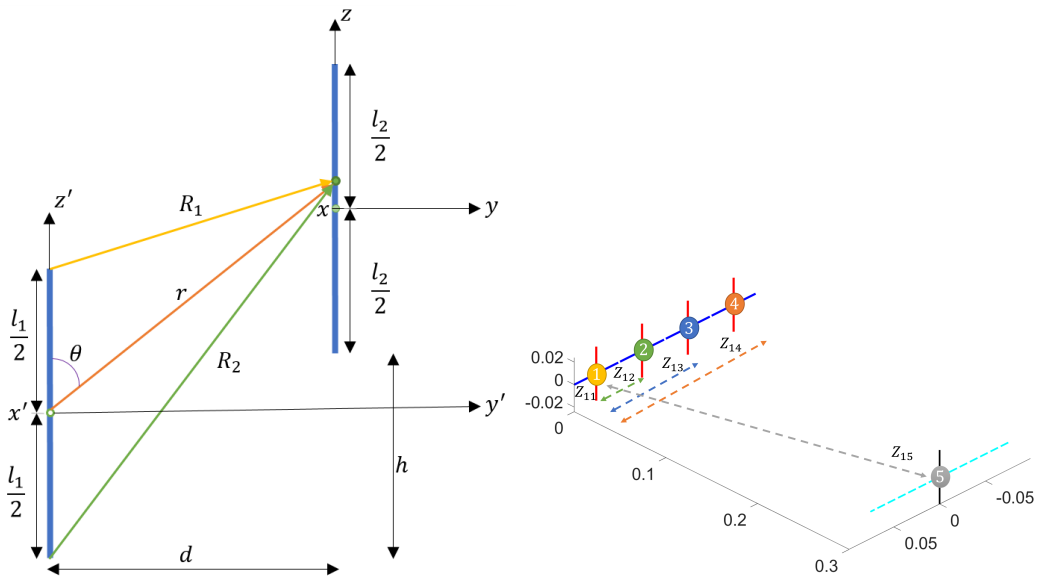

(a) Dipole positioning length calculation (b) Impedance matrix **Z** calculation

Figure 4.2: Simulation procedure to determine dipole distance for calculating mutual impedance between them. From [95], ©IEEE

If two antenna have different spacing and length then the mutual impedance is given by

$$Z_{21i} = j\frac{30}{\sin(\frac{kl_1}{2})\sin(\frac{kl_2}{2})}\int_{-\frac{l_2}{2}}^{\frac{l_2}{2}} \sin\left[k(\frac{l_2}{2} - |z^{'}|)\right] \left[\frac{\exp(-jkR_1)}{R_1} + \frac{\exp(-jkR_2)}{R_2} - 2\cos(\frac{kl_1}{2})\frac{\exp(-jkr)}{r}\right] dz^{'} \ . \tag{4.10}$$

It can be determined from Figure 4.2a (from [94], ©IEEE) that

$$\begin{aligned} R_1 &= \sqrt{X^2 + Y^2 + Z^2 + (Z - \frac{l}{2})^2} = \sqrt{d^2 + (Z - \frac{l}{2})^2} \\ r &= \sqrt{X^2 + Y^2 + Z^2 + Z^2} = \sqrt{d^2 + (Z + l)^2} \\ R_2 &= \sqrt{X^2 + Y^2 + Z^2 + (Z + \frac{l}{2})^2} = \sqrt{d^2 + (Z + \frac{l}{2})^2} \end{aligned} \ , \tag{4.11}$$

where d is the distance between two elements, l_1, l_2 are the length of the two

dipole. The wave number is defined by $k = \frac{2\pi}{\lambda}$. Integrating the equation 4.11 will provide the mutual impedance of two different dipole. However, for the identical dipoles a straight forward equation is available and given in [96] for side by side configuration as

$$\begin{aligned} R_{21m} &= \frac{\eta}{4\pi}[2C_i(u_0) - C_i(u_1) - C_i(u_2)] \\ X_{21m} &= -\frac{\eta}{4\pi}[2S_i(u_0) - S_i(u_1) - S_i(u_2)] \\ u_0 &= kd \\ u_1 &= k(\sqrt{d^2 + l^2} + l) \\ u_2 &= k(\sqrt{d^2 + l^2} - l) \\ Z_{21m} &= R_{21m} + jX_{21m} \\ Z_{21i} &= \frac{Z_{21m}}{\sin^2(\frac{kl}{2})} \end{aligned} \quad . \tag{4.12}$$

4.1.4 Generating Z and S Matrices

Once all the necessary values of self and mutual impedance were calculated, the impedance matrix **Z** can be populated by their corresponding values as shown in Figure 4.2b. Now, from the [**Z**] matrix calculated from the above-mentioned technique, the **S**-parameters can be calculated, normalized to the characteristic impedance Z_0 as

$$[\mathbf{S}] = ([\mathbf{Z}] + \mathbf{Z_0}[\mathbf{U}])^{-\mathbf{1}}([\mathbf{Z}] - \mathbf{Z_0}[\mathbf{U}]) \ , \tag{4.13}$$

where [**U**] is the identity matrix and **Z** is the impedance matrix. The whole system **S** parameter matrix, including probe array interaction, is calculated. It is possible to quantify the coupling associated with elements, using the sand-box, to generate the "ground-truth" pattern for the array. Also, it is possible

to analyze the probe response for a probe being in the quasi-near-field.

4.1.5 Validating the Sand-box

To ensure the validity of the sand-box, the mutual impedance of two side by side collinear $\frac{\lambda}{2}$ dipoles is compared by using the induced EMF method. The reference graph, in Figure 4.3a, and simulated graph, in Figure 4.3a, matched exactly providing the validity of the sand-box. The reference graph is taken from a textbook [31]. From the Figure 4.3 it is validated that the reference

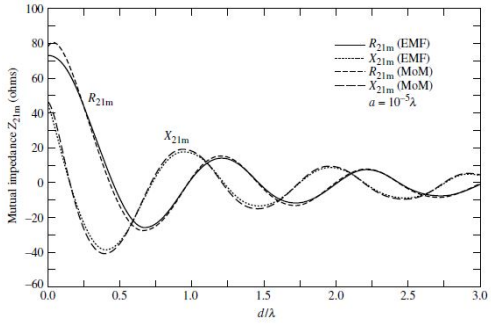

(a) Mutual Impedance Reference [96]

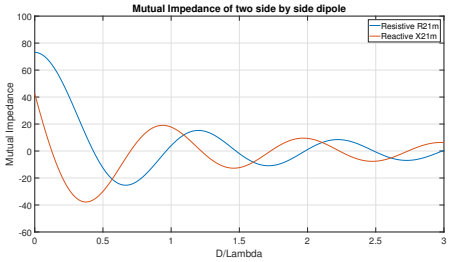

(b) Simulated Mutual Impedance from the Sand-box

Figure 4.3: Mutual impedance of two side-by-side $\frac{\lambda}{2}$ dipoles using induced EMF Method

and the simulated plot agree with each other hence, the sand-box provides the exact **Z** matrix for dipole antennas.

4.1.6 Features of Sand-box

In Figure 4.4 a 15×15 array panel with a single element probe is simulated. The parameters are set as an ideal dipole with 0.5λ length and 0.5λ spacing, and 3 GHz frequency. However, using the sand-box, one can go any arbitrary choice of their own. Figure 4.4 shows relative signal strength when the probe is mounted in the corner of the array. The distance between the probe and each element is not constant, so each element in Figure 4.4 is color-coded according to the relative signal strength that the array (or probe) will receive. It is noticeable that the element closer to the probe received a strong signal, and the further the element is, the lesser the signal strength.

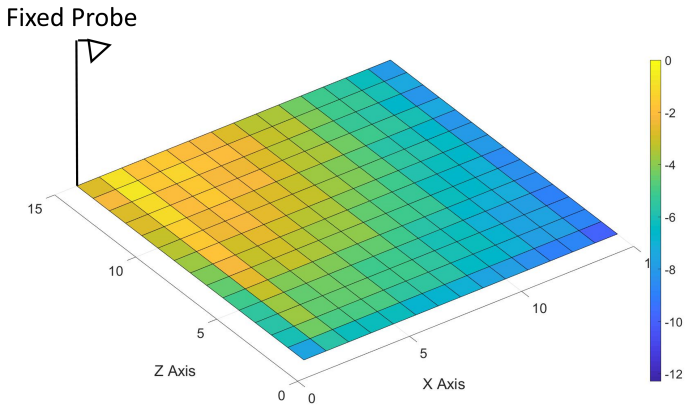

Figure 4.4: Relative signal strength on a 15×15 array panel by illuminating an on-board calibration probe

Another phased array issue of corner element and center element needed to be discussed. It is known that the center element has a periodic environment and behave differently than corner elements. This difference also varies on the array panel size. Depending on the size of the array, a "large array assumption" can be made. The basic array element field pattern is the prod-

uct of the isolated element pattern and a space factor that accounts for all of the other coupled elements. In Figure 4.5a a 9×9 array was considered. Here the embedded element pattern is compared with the ideal pattern of the array. A maximum difference of 3 dB has been noticed. In Figure 4.5b, the corner element embedded pattern was simulated with the same configuration as Figure 4.5a. Corner element has a maximum difference of almost 8 dB. Also, the corner element standard deviation is larger than the center element. For simulating a large array, a 15×15 array was simulated and plotted in Figure 4.5c. As expected, it is noticeable that there is much better agreement between the ideal and embedded center element pattern with the larger array. These graphs also portray the sand-box's usefulness since these are similar to [97].

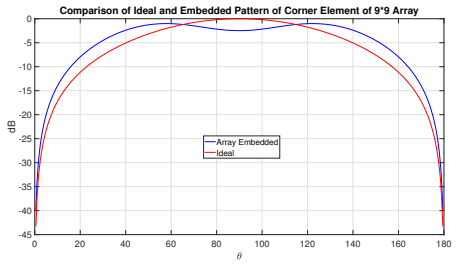

(a) Center element of 3×3 array

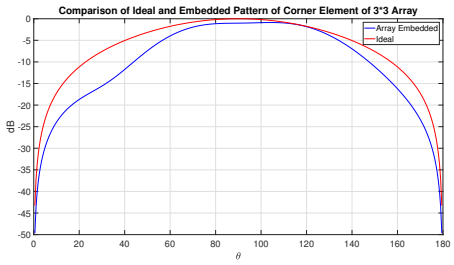

(b) Corner element of 3×3 array

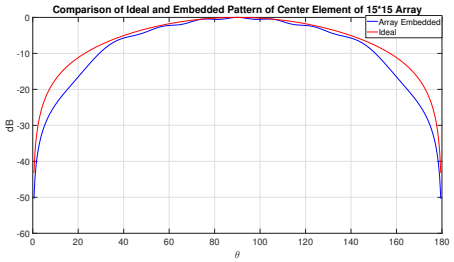

(c) Center element of 15×15 array

Figure 4.5: Internal calibration using technique/equipment which will be fielded with the system

Figure 4.6c, the phase progression of the antenna element with a probe

in the corner of the array was plotted. As discussed earlier, the waves could not be considered plane waves since the probe is in the quasi-near-field. As expected, the phase wrapping between $-180°$ to $180°$ is visible in the plot.

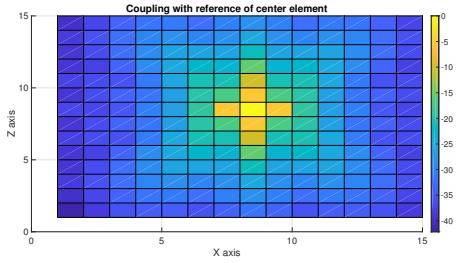

(a) Center element of 3×3 array

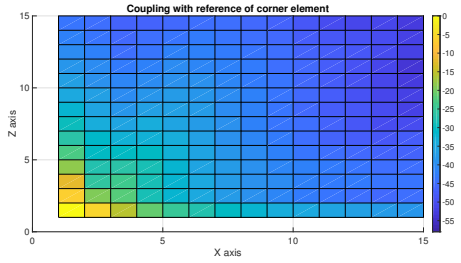

(b) Corner element of 3×3 array

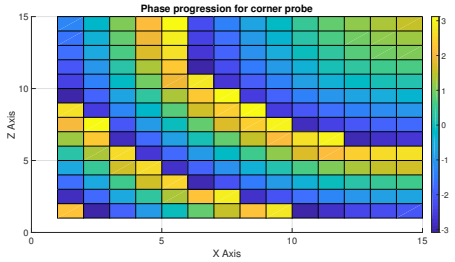

(c) Center element of 15×15 array

Figure 4.6: Coupling between the adjacent elements from the simulation sandbox, and phase progression from the near-field probe

The coupling between the elements will be analyzed since it plays significant role in element pattern ripples. First, the center element of a 15×15 array antenna is considered as depicted in Figure 4.6a. The center element is strongly coupled to the adjacent elements as expected. One of the corner elements of the same array is also considered. It is noticeable that the coupling of a corner element will be different than the center element due to lack of periodicity. It is a common practice to fill out one or two rows of passive elements over the active element of the array to mitigate the effect of this discontinuity.

4.2 Calibration Procedure

4.2.1 System Settings

To demonstrate the proposed fast calibration method, a linear array consisting of 13 elements is considered. The dipole length was chosen as 0.48λ and vertically placed along the z axis. The elements were placed along the x axis. The spacing between the elements is $\frac{\lambda}{2}$. The frequency was chosen as 3 GHz. A single dipole was chosen for the probe, which has a similar configuration to the array dipole. Two different distances, 3λ, in Figure 4.7a, (from [94], ©IEEE), and 10λ, in Figure 4.7b were selected for probe position along with y axis of the array. A typical configuration for the system, as shown in Figure 4.7.

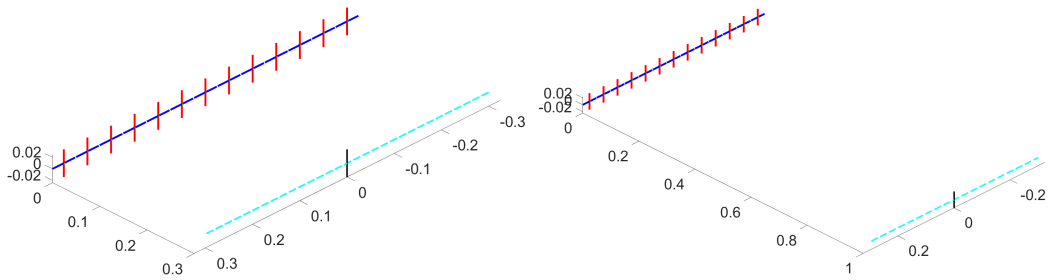

(a) Probe placed in 3λ distance (b) Probe placed in 10λ distance

Figure 4.7: Virtual framework of 13 element array for calibration purpose. From [94], ©IEEE

For calibrating the array, a step-by-step procedure was followed. First, the complex probe element response b'_n is calculated for each array element by using the **S** parameters as shown in Figure 4.8a, (From [94], ©IEEE). If the array is full digital, b'_n can be measured directly as every element has a T/R module for transmitting and receive. If the array is analog, the CCE technique can be used to generate b'_n. Using this complex weight of b'_n, the uncalibrated pattern is calculated. Second, the compensation b''_n needed to be calculated to

calibrate the array, as shown in Figure 4.8b. Finally, the complex correction weight for each element b_n^c is calculated to construct the calibrated pattern.

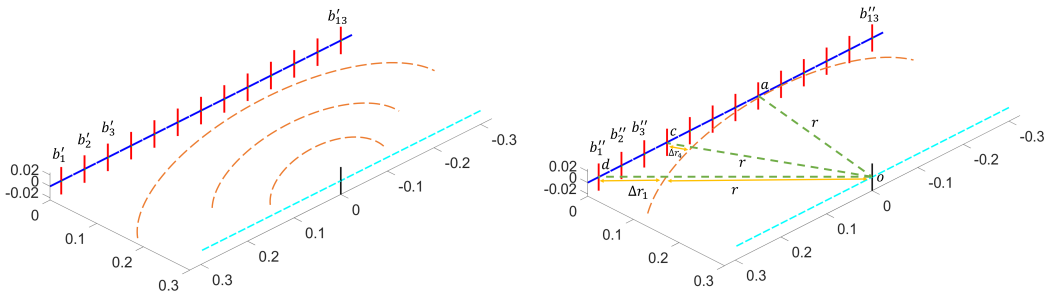

(a) Calculation of $b_n^{'}$ (b) Calculation of $b_n^{''}$

Figure 4.8: Error model and calibration weight generator geometry. After [94], ©IEEE

4.2.2 Error Modeling

Usually an approximation, probe being in the far-field, has chosen to calculate the pattern of an array considering incoming wave as plane wave. In the proposed technique, the probe was actually stationed at quasi-near-field. So the assumption of having a plane wave in front of an array is no longer valid, and we need to compensate for that.

4.2.2.1 Amplitude and Phase Correction

With the assumption of the probe being in the far-field, a plane wave in front of the array can be considered. In reality, the waves are not planar, rather they have a spherical wave front [94] as shown in Figure 4.8b. As a result, a correction in phase is necessary. Here, for a spherical wave front, the radius is r and the extra part Δr is responsible for the plane wave displacement. For phase correction, it is needed to be compensated by $R_n = r + \Delta r_n$ where $n = 1$ to 13 for this specific case. Now to find out the value of Δr the equation of

right triangle *oad* from Figure 4.8b can be solved as

$$(r + \Delta r)^2 = r^2 + (ad)^2 \ , \tag{4.14}$$

neglecting the $(\Delta r)^2$, since it is too small and has negligible effect, equation 4.14 become

$$\Delta r = \frac{(ad)^2}{2r} \ . \tag{4.15}$$

As the dimension of $\vec{ad}$ is already known, Δr can be obtained for each element of the array. Once the Δr is available for each element, $R_n = r + \Delta r_n$ can be calculated. The phase correction with R_n is now possible. So the phase of the front also changes due to the plane wave assumption. The individual R_n was calculated. The phase correction can be quantified as

$$c_n = e^{jkR_n} \ . \tag{4.16}$$

Mathematically, for phase and amplitude correction, complex weight can be generated by using

$$b''_n = \frac{e^{jkR_n}}{R_n} \ . \tag{4.17}$$

Corrected complex weight to calibrate the array can be generated by using $b^c_n = b'_n \times b''_n$. This complex value can compensate for both the amplitude and phase of the received signal from the probe. Once the probe is transmitting, the complex signal can be received in each element and compensate them with the corrected complex weight b^c_n to calibrate the array.

4.2.2.2 Virtual Probe Location

In reality, phased arrays are getting smaller with the increasing demand for the high-frequency antenna. Practically, it is challenging to identify the probe location to calculate the complex weight precisely. The possibility of introducing an error while calculating the exact probe location is extremely high. In [94], a fixed probe-based calibration scheme using the exact probe position was introduced. However, while taking the actual measurement, that proposition was subject to unintentional error and cumbersome distance measurement, which is not aligned with the fast calibration method. In this dissertation, a new method is proposed to relax the knowledge of the exact probe location. This approach can identify the probe position through an algorithm inside the virtual box.

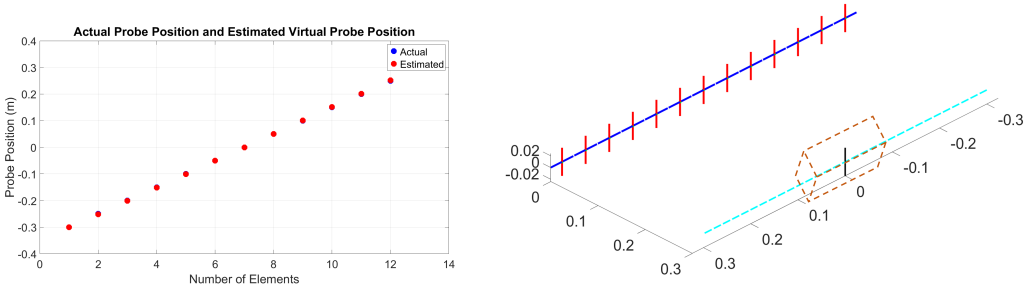

(a) Actual and virtual probe position (b) Creating a virtual box to find the probe position

Figure 4.9: Use of virtual box to calculate the probe position virtually and showing the actual and virtual probe location. From [95], ©IEEE

In order to implement this algorithm, first a virtual box surrounding the probe is created, as shown in Figure 4.9b, (from [95], ©IEEE). First, the probe response b'_n is measured. Then, the virtual box surrounding the probe is created. Next, b''_n is calculated for each virtual position of the probe. After that, corrected weight $b^c_n = b'_n \times b''_n$ is calculated. Now, the maximum value

of $|\sum b_n^c|$ needs to be quantified for different positions to optimize the system. When the value of $max(|\sum b_n^c|)$ is optimized, the probe location can be determined. The corresponding b_n^c is used to calculate the complex weight for each element. Figure 4.9a portrays the performance of the virtual probe location compared to actual probe location. The error is minimal (close to 0.4%) between the estimation and the actual probe position.

4.3 Simulated Ground Truth, Uncalibrated and Calibrated Pattern

4.3.1 "Ground-Truth" Pattern

First, the "ground-truth" pattern for the linear 13 element array without the probe was simulated, by calculating the complex weight, using $[b_n] = [\mathbf{S}][a_n]$. Unit amplitude excitation for all the elements as a_n were selected. After the complex values of b_n for AUT, elements were determined, these values were used to calculate the "ground-truth" pattern for the array. The geometry used to generate the pattern is given in Figure 4.8. This is represented in blue color in all the graphs used, as shown in Figure 4.10a.

4.3.2 Uncalibrated Pattern

Second, the uncalibrated pattern was calculated. In order to determine the uncalibrated pattern, the equation $[b'_n] = [\mathbf{S}][a'_n]$ was used. This time a_n has all zero values, except the probe has unit amplitude. This can provide the interaction of elements with probe only. From this equation, complex probe responses of the array element b'_n were obtained by which the uncalibrated

pattern for the array was calculated.

4.3.3 Corrected Pattern

Third, the correction needed for the uncalibrated pattern, to make it close to the "ground-truth" value, was calculated by using amplitude and phase correction b_n'' as mentioned in equation 4.17. Then the complex corrected weights of each element, $b_n^c = b_n' \times b_n''$ were determined and used to simulate the calibrated pattern.

4.3.4 Result and Discussion

First, the "ground-truth" and the uncalibrated pattern is simulated by keeping the probe 3λ distance in $x-z$ plane in front of the center element of the array as shown in Figure 4.7a. After that, the virtual probe location algorithm found the same position for the array and compensated according to complex weight. The patterns are depicted in Figure 4.10a, (from [94], ©IEEE).

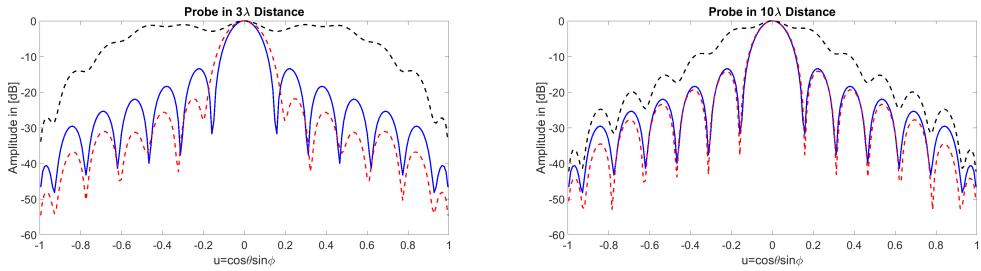

(a) Pattern with 3λ distance probe (b) Pattern with 10λ distance probe

Figure 4.10: Ground turth, uncalibrated and calibrated pattern from 3λ and 10λ distance to compare the difference between near-field probe and quasi-near-field probe distance. From [95], ©IEEE

There is a noticeable pattern mismatch. Next, with the same set-up of simulation, the probe was placed in quasi-near-field at 10λ distance. In Fig-

ure 4.10b, a much better agreement of ground-truth and the calibrated pattern can clearly be observed, which is expected.

One of the phased array antennas' critical features is its capability of electronically steering the main beam. Now a scanning angle of 45∘ was simulated. For scanning, Taylor taper coefficients of -25 dB side-lobe level were used. First, the probe was centered at 3λ distance. The geometry was similar to Figure 4.7, and the simulation result is shown in Figure 4.11a, (from [94], ©IEEE).

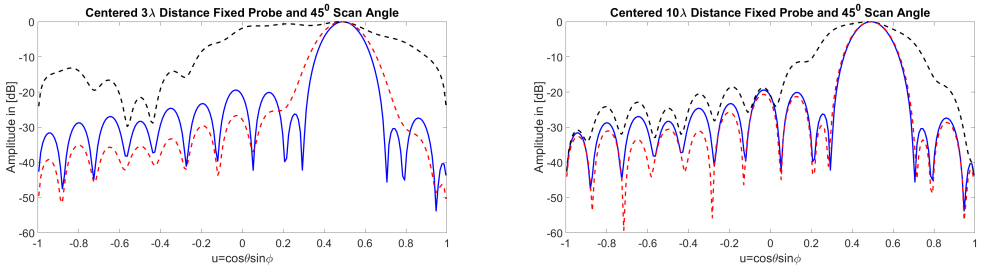

(a) Pattern with 3λ distance probe (b) Pattern with 10λ distance probe

Figure 4.11: Ground turth, uncalibrated and calibrated pattern for a scanning angle of 45° from 3λ and 10λ distance to compare the difference between near-field probe and quasi-near-field probe distance. From [95], ©IEEE

There is an apparent disagreement of calibrated, and "ground-truth" pattern noticed due to the probe being too close in front of the array. However, if the probe is taken further away, the simulation seems to match reasonably with "ground-truth". For example, if the probe position is 10λ apart, then the beam pattern started to align with the "ground-truth" as seen in Figure 4.11b. It is also worthy to note that the beamwidth is increased while scanning, which is expected.

Finally, the probe was placed to the extreme left of the array geometry instead of the center. We took two scenarios, for 3λ and 10λ distance. In Figure 4.12a, (from [94], ©IEEE), the probe is in 3λ distance, and the cali-

brated pattern is not in a good agreement with "ground-truth". However, in Figure 4.12b the probe is in 10λ distance, and an excellent agreement between calibrated and "ground-truth" pattern is observed.

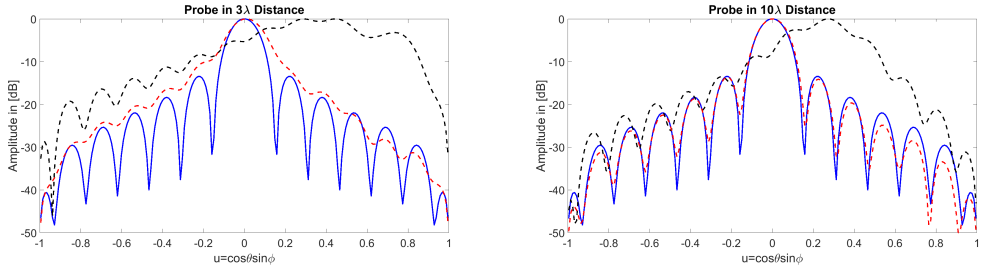

(a) Pattern with 3λ distance probe (b) Pattern with 10λ distance probe

Figure 4.12: Ground truth, uncalibrated and calibrated pattern from 3λ and 10λ distance cornered probe to test the capacity of probe position From [95], ©IEEE

As shown above, all the examples have a better result for the probe being placed in quasi-near-field after the compensation over the near-field probe position. Also, the virtual probe location-based algorithm is working as expected.

4.4 Chapter Summary

In this chapter, the proposed model is simulated by using ®Matlab sand-box. Step by step procedure to develop this toolbox is explained. Complex calculation of self-impedance and mutual impedance are demonstrated. Then the sand-box is validated by comparing it with known parameters and also showed some of the features of the sand-box. Next, the calibration procedure is explained briefly and demonstrated for two probe positions 3λ distance and 10λ distance. Ground truth, uncalibrated, and calibrated patterns are simulated. Keeping the probe in 10λ distance generates the pattern very close

to the ground truth. Since in this chapter, the simulation proves the proposed calibration procedure, in the next chapter, the actual measurement will be conducted using a k_u band phased array inside a custom made range.

Chapter 5

Measurement and Validation of the Proposed Theory

As mentioned in Chapter 2, the overall calibration procedure can be divided into two steps, initial and in-situ [98]. The name itself suggested that initial calibration is the first alignment checking process after manufacturing the array to account for all systemic and random errors associated with different components of the RF chain. After initial calibration, phased array antennas are subject to the secondary parameter related errors, and it is needed to be monitored frequently after deployed. This is termed as in-situ calibration.

Typically, initial calibration would be performed immediately after fabrication and requires specialized tools, such as an anechoic chamber, positioner, etc. An exhaustive literature review is provided in Section 2.2 on different calibration approaches available. However, the need for fast and accurate calibration techniques is increasing rapidly with the increasing trend of using low

cost phased array in various domains. Especially in satellite, onboard antennas, and satellite user terminal antennas in the ground need quick and accurate calibration methods. Any downtime can significantly affect their operation in terms of revenue. Also, the upfront calibration time directly affects the cost of the terminal. For example, if one million user terminals being produced a year, there will be a need for at least five hundred near-field ranges in any given time for calibrating those units, which is not feasible. Irrespective of the method being used, an initial calibration usually takes a great deal of time. In Chapter 3, a theory of the novel calibration method was introduced using a fixed probe, which can minimize the calibration procedure within 20 minutes. In Chapter 4, the simulation of the proposed theory is presented. Simulation provides us with a promising result. In this chapter, the actual measurement and validation of the proposed theory will be offered.

5.1 System Description

Collins Aerospace has supported this project. The phased array we have used for the measurement and validation is the property of Collins Aerospace. Since this is a proprietary system, it is not possible to show the detailed diagram or figure of the existing system in this dissertation. However, in this report, some information has been provided to get an idea about the system with their permission. The system is a satellite user terminal prepared for ground operation and communication with the lower earth orbital (LEO) satellite network. However, it is worth mentioning that the proposed technique can be applied to any array that fits the proposed fast calibration technique's scope. The entire measurement process took place in Cedar Rapids, Iowa, at the Collins Aerospace antenna test range facilities.

First, a fixed probe-based calibration procedure is performed. For the measurement performance, a custom made 46×46 inch wooden box was created. The whole setup is depicted in Figure 5.1. The box was populated with microwave absorber foam blocks to reduce multi-path effects and create a quiet zone on the face of the array for the initial calibration. The probe was placed in the quasi-near-field distance approximately 50λ away from the antenna under test (AUT). It was a dual-polarized circular waveguide probe with a choke ring. The probe frequency range was 10 to 15 GHz.

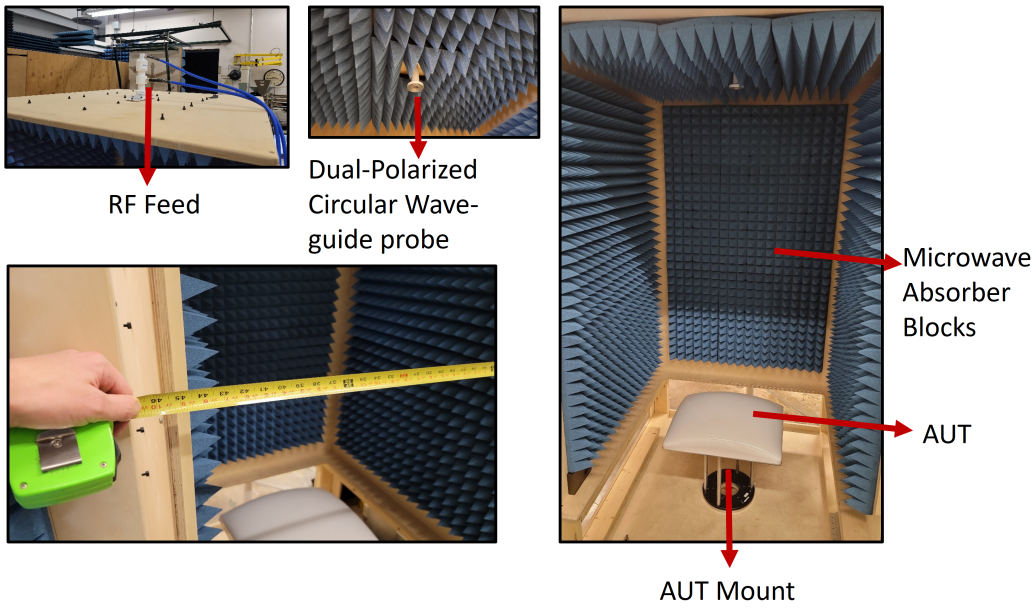

Figure 5.1: Setup of 512 element array fast calibration method with a fixed probe. The arrangement remains same for the whole measurement period for generating calibration co-efficient

The probe and AUT are both dual-polarized, but in this dissertation, only H polarization is used to make proof of concept of the proposed theory. However, one can notice from Figure 5.1 RF feed that the arrangement is available for dual pole calibration.

The AESA system is proprietary equipment of Collins Aerospace; only

allowed information for the system is provided. The antenna has four units. Two of them used to receive and two for transmit. In this report, a small part of two receive antenna unit is used to avoid any intellectual property conflict. A total of 512 element has been used to validate the proposed theory. Figure 5.2 a brief block diagram of the antenna under test is provided.

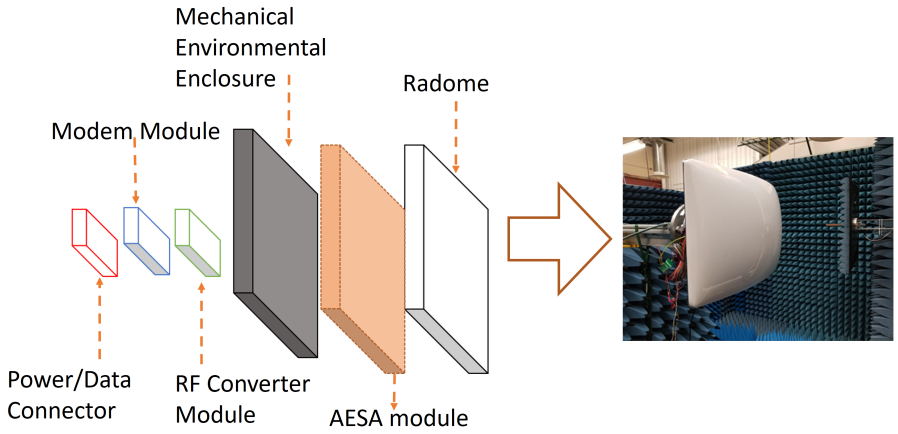

(a)

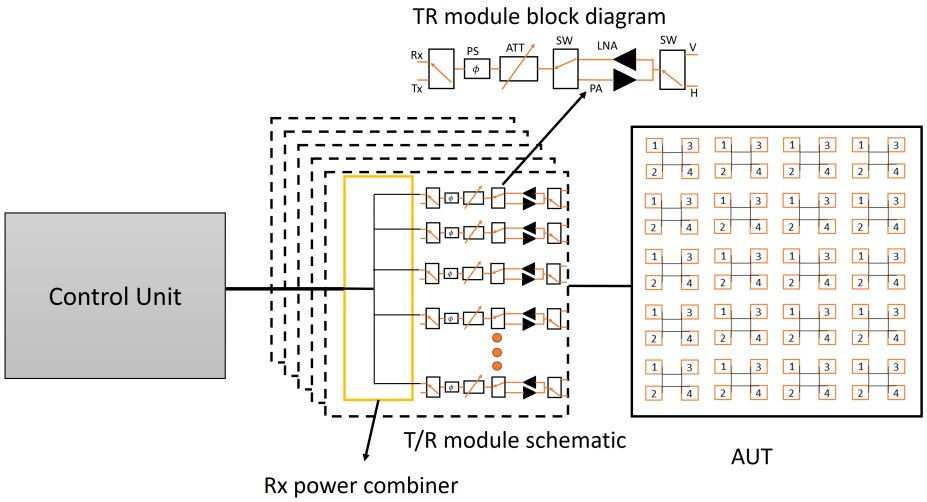

(b)

Figure 5.2: Description of the phased array antenna system. (a) provides a major assembly block diagram for the ESA and (b) shows the block diagram of the antenna under test with TR module and controller unit.

In Figure 5.2a, major sub-assemblies is shown, which comprises of Power and data connector, modem module, RF converter module, environmental enclosure, AESA module, and radome to protect the system. The system contains all the components packed and made into one compact system, as shown in Figure 5.2a. In Figure 5.2b a brief block diagram of the array is given, which comprise of the TR module including phase and amplitude controller, LNA, power amplifier (PA), and the switching circuit. Please keep in mind that this is not an actual block diagram of the system instead of a rough block diagram to portray similar operational arrangements. There are two receive antenna units used for the measurements. Two units are designed in a way that there is a 180° phase shift between the two panels. Also, there is a gap between the two panels. All of these phenomena will be noticed in the upcoming analysis.

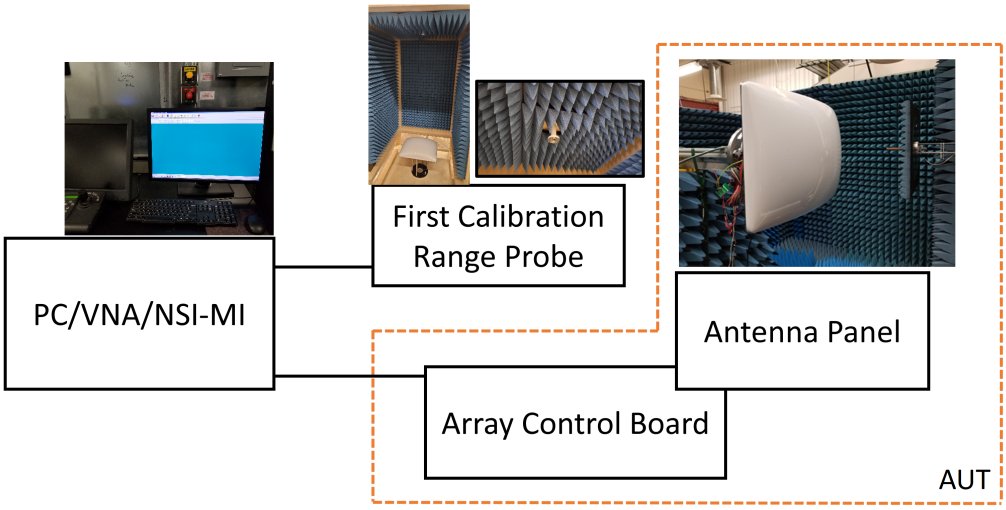

Figure 5.3: Block diagram of the experimental setup including main components and instruments needed for fast calibration.

In Figure 5.3, the high level experimental setup is depicted. The antenna panel and array control board together was placed on the floor of the box. The

probe is being attached to the ceiling of the box in the quasi-near-field. The probe is a dual-polarized circular waveguide with a choke. The antennas are made for half-duplex operation, with a frequency range of $10.7 - 12.7$ GHz for receive and $14 - 14.5$ GHz for transmitting. The system is linearly polarized. The antenna elements are placed $\frac{\lambda}{2}$ distance apart using the highest frequency possible. For calibration purposes, a VNA is needed to take the measurements and store them.

5.2 Fast Calibration using CCE

5.2.1 Initial Calibration

The system used for the validation is not a full digital array, so it is needed to implement the CCE technique for initial calibration, which is explained in Section 3.4.1. The capability of measuring all elements simultaneously is far more advantageous over the single element technique (e.g., park and probe) for analog arrays. Furthermore, the CCE technique is also N times faster than mutual coupling based calibration techniques, as the extraction of each element's excitation is the post-processing of the decoding technique. CCE technique is also capable of detecting dead elements in the array. The instrumental setup is shown in In Figure 5.3. Readers can notice, this setup requires minimum equipment such as a computer, VNA, and quasi-near-field compact range. The VGAs are needed to be configured with Hadamard matrix reference for encoding purposes while receiving signals from the probe. Once the signals are received, by using the orthogonality property of the Hadamard matrix, the individual element level complex excitation can be decoded. Using the virtual probe algorithm, the b_n'' will be calculated for a specific probe position.

In Figure 5.4, the uncalibrated and calibrated pattern of the antenna is presented. There are a couple of things that needed to be noticed from this plot. As mentioned before, the antenna used for these measurements has two units, which has 180° phase offset between them. Also, there is an existing gap between the two panels, which are not populated by the array elements. In Figure 5.4a, some ripples in the side-lobes are visible, which is coming from the gap. The elements adjacent to the gap acted as corner element for both the units. Moreover, it is noticeable that two main beams are coming from the 2D uncalibrated pattern. The reason for the two main beam is the phase offset between the panels.

The black dashed line in the Figure 5.4b represents the −13 dB SLL level. The uncalibrated pattern is almost 5.8 dB above the level, with the first null in the elevation cut became broader. However, after calibration, the −13 dB SLL level has been achieved in the elevation cut, and in the azimuth cut, the SLL is around −11.5 dB. This is because the gap between the two panels exists in the azimuth plane, not in the elevation plane. In Figure 5.4b, the calibrated pattern is visible. It is noticeable that the first null's width reduced greatly in the elevation plane, making the main beam more directive. Also, after calibration, there is only one main beam instead of two in the uncalibrated pattern. From Figure 5.4, it is noticeable how the beam is shaped after the initial calibration.

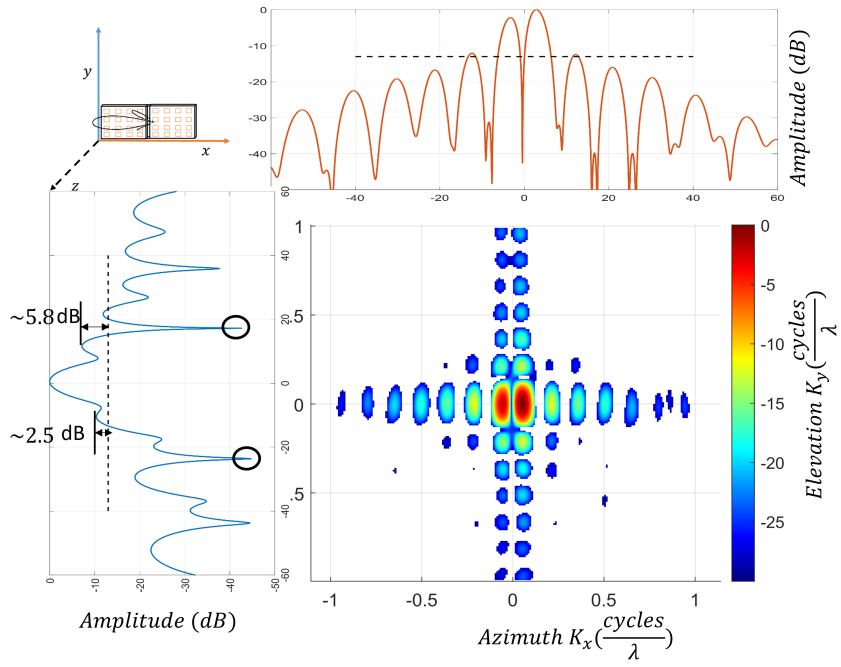

(a)

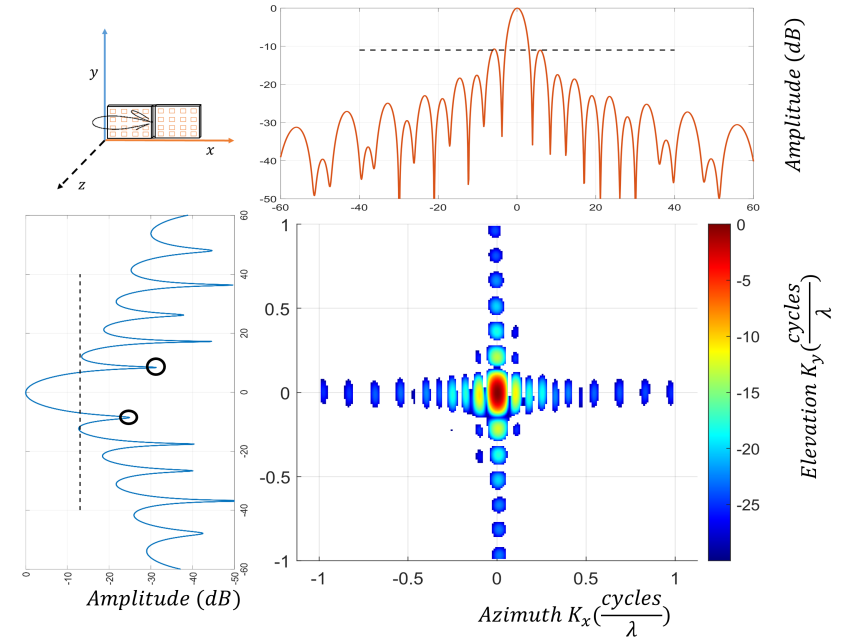

(b)

Figure 5.4: Measured boresight antenna pattern on H-polarization, uniformly illuminated for 512 element array. (a) Uncalibrated array pattern without any compensation, including elevation and azimuth cut; and (b) is the compensated calibrated pattern. The dashed black line represents the peak side-lobe level of each cut.

From an antenna engineer's perspective, it is also important to analyze the hologram of the array in the aperture of the AUT. Holograms provide important information about each element's behaviors on the antenna aperture. Figure 5.5 shows the hologram of the array before and after calibration. Figure 5.5a depicts the hologram of amplitude variation before and after calibration. The first thing to be noticed is the dead elements of the panel. These dead elements are showing -40 dB of amplitude. So with this calibration procedure, successful detection of the dead elements is possible. Also, readers can notice the wide variation of amplitude got minimized after the calibration. To quantify this, the root mean square error has been calculated. Before calibration, the RMSE was found around 1.5 dB, whereas, after calibration, it was 0.65 dB. A linear comparison is depicted in Figure 5.5a. In the phase hologram, some exciting changes have been noticed. First, in Figure 5.5b, the dead elements can be detected as those are not aligned with phase. In the uncalibrated phase hologram, the phase offset between the two panels is also visible. However, after calibration, they all became aligned except the dead elements. The variation after calibration is approximately 5°, which was 42° before calibration.

5.2.2 Scanning and Amplitude Tapering

After the initial calibration, some phased array characteristics, such as beam steering and side-lobe tapering, are performed to identify the robustness of the proposed fast calibration technique. To validate this, three different operations are performed with the calibrated array.

First, beam steering is conducted by varying the azimuth angle to 45° and keeping the elevation angle at the boresight. Next, another scanning is per-

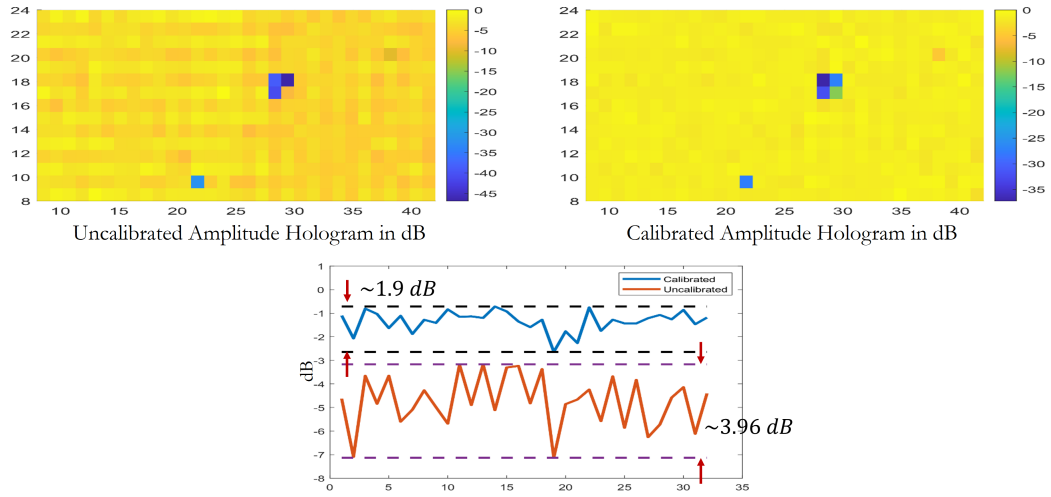

(a)

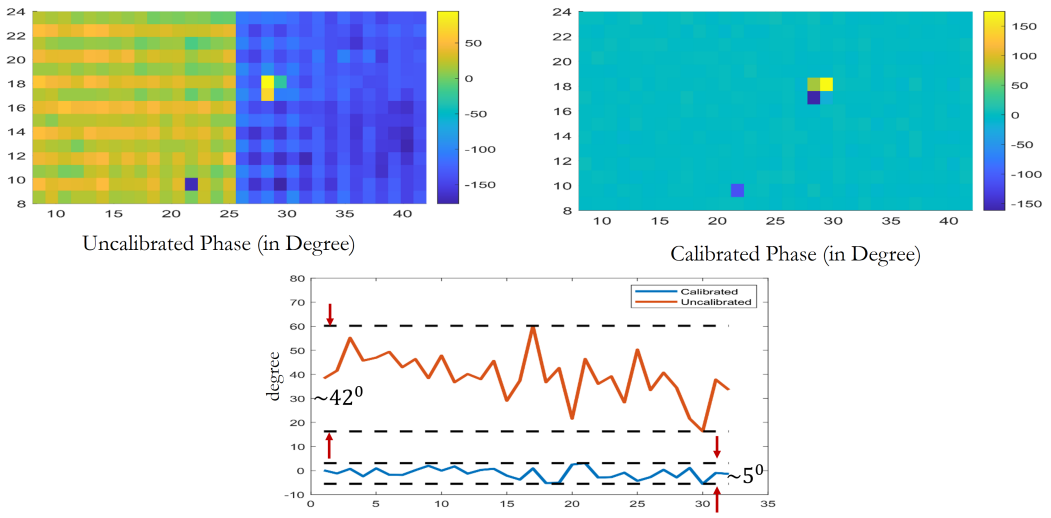

(b)

Figure 5.5: Measured hologram of the antenna under test (a) uncalibrated and calibrated amplitude hologram showing the variation; and (b) uncalibrated and calibrated phase hologram showing the variation. The dashed black line represent the variation range

formed with the 45° azimuth and 45° elevation angle to observe the beam shape. In Figure 5.6, these two scenarios are plotted. First, in Figure 5.6a the scan angle is in the azimuth 45°. It can be noticed from the 2 D plot that the main beam is shifted towards the azimuth angle. While scanning, broadening

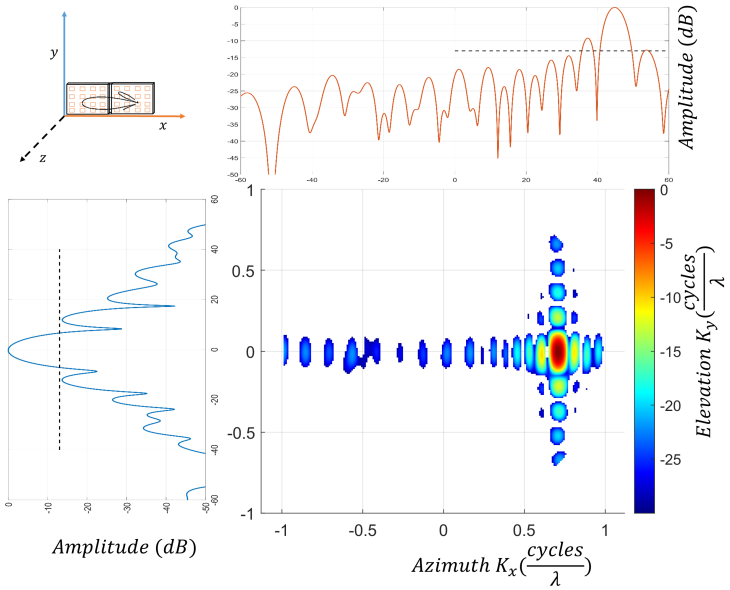

(a)

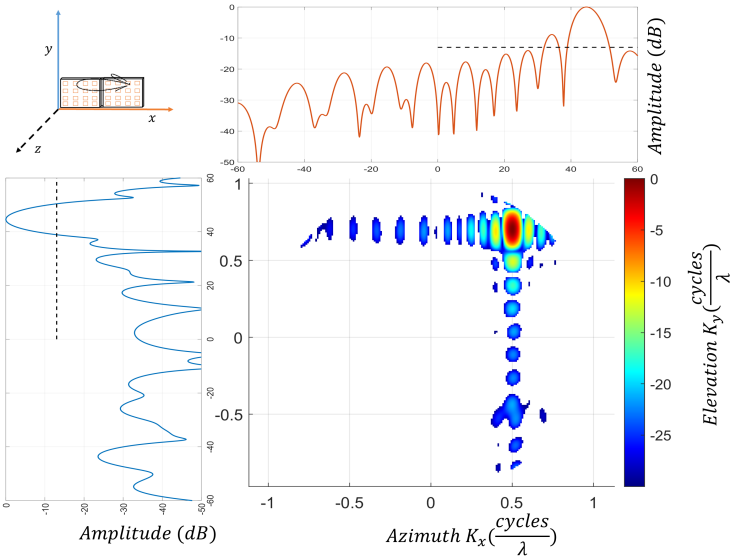

(b)

Figure 5.6: Measured antenna pattern on H-polarization, for electronic scanning angle. (a) the array is scanning at 45° scanning angle in azimuth; and (b) is the scanning angle of 45° azimuth and 45° elevation angle. The dashed black line represent the peak side-lobe level of each cut.

of the main beam and increase of SLL level were incurred as expected. However, it is observed that in the elevation cut, the SLL remains in the −13 dB

level.

In the Figure 5.6b, the beam is scanned at 45° azimuth and 45° elevation angle. As seen from the plots that the main beam is moving along the direction. This time both the azimuth cut and elevation cut shifted towards 45°. It is noticeable that the SLL remains below −13 dB for the elevation cut but marginally increased in the azimuth cut. As mentioned earlier, there is a gap between two panels in the azimuth plane. It may be the reason for the SLL level in the azimuth plane. Another advantage of the phased array is

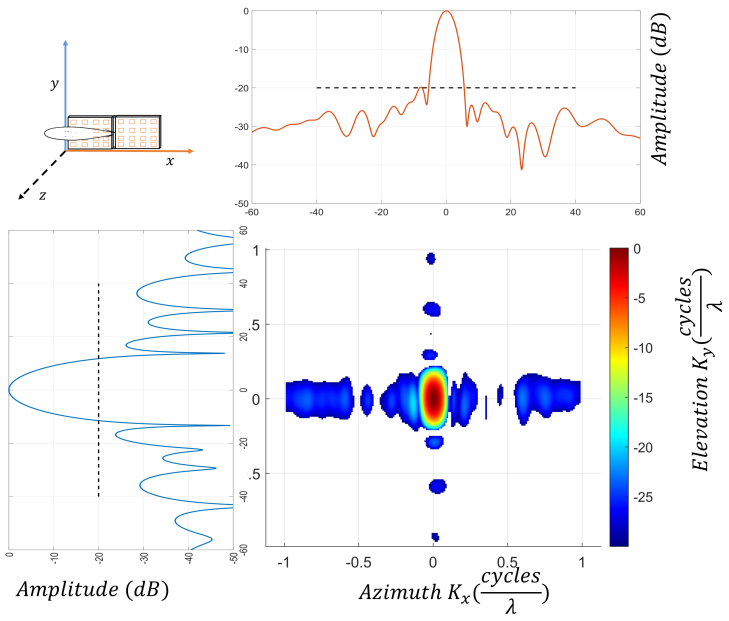

Figure 5.7: Measured antenna pattern in boresight with −20 dB Taylor tapering to reduce the side-lobe level of the array pattern.

tapering the side-lobe level so that unwanted energy will not be radiated from the antenna. This is basically done by controlling the amplitude of the phased array elements in a way that center elements get strong excitation than the corner elements. The final characteristic is conducting a side-lobe tapering with the calibrated array. One famous option to reduce the side-lobe level is

using Taylor tapering. Here -20 dB Taylor tapering is used, and the beam pattern is shown in Figure 5.7. It is noticeable how most of the energy radiated from the center of the array in the far-field. By observing the elevation and azimuth cut, it can be confirmed that all the side-lobes are below the -20 dB level as expected.

5.3 NF Chamber Measurement

The calibration so far discussed was done using a fixed probe in the quasi-near-field chamber. Though the patterns and overall results are satisfactory, another set of measurements is taken for validation purposes in the near-field chamber using the calibration weights generated from the proposed fast calibration technique. Near-field measurements are widely acceptable to industry and academia for measurement accuracy.

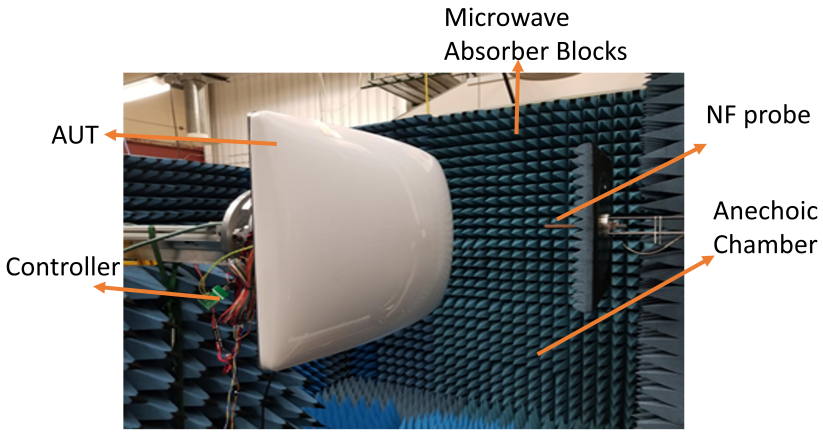

Figure 5.8: Near-field chamber set up for the array measurement to validate the proposed fast calibration technique

Figure 5.8 shows the arrangements made for measuring the array. The frequency sweep range was $10.7 - 12.7$ GHz, and the calibration weight was

applied for 11.7 GHz.

5.3.1 Far-field Gain Pattern Measurement

The far-field gain pattern measurement for the uncalibrated and calibrated pattern is shown in Figure 5.9. These patterns portrayed similar characteristics, as shown in the Figure 5.4a. Though elevation cut maintains the SLL at -13 dB, it is marginally higher in the azimuth plane due to a gap between two panels. The uncalibrated pattern and calibrated pattern is taken in two different ranges, quasi-near-field compact range and near-field range poses the same characteristics in terms of beam pointing, side-lobe level, and beamwidth. This can effectively confirm the validation of the proposed model. Also, there are ripples present in the side-lobe for both calibrated and uncalibrated patterns, which is due to the gap between two panels in the azimuth plane. As there is no gap in the elevation plane, no ripple is observed. Figure 5.9b also shows the development in the pattern symmetry compare to the uncalibrated pattern in the azimuth plane, which is important as with the uncalibrated pattern, the SLL on the left side is much higher than the right side. Looking at the NF measurements with the calibration weights applied, it is safe to say that the fast calibration technique is playing its role in the calibration.

5.3.2 Hologram of the Array

After the far-field pattern, another significant tool is to plot the hologram of the array to observe the elements on the array aperture. In Figure 5.10, the hologram of the phased array calibrated and uncalibrated pattern for amplitude and phase is depicted. As mentioned earlier, the tow panel of the used system has 180° phase shift. To make a valid comparison, a manual 180°

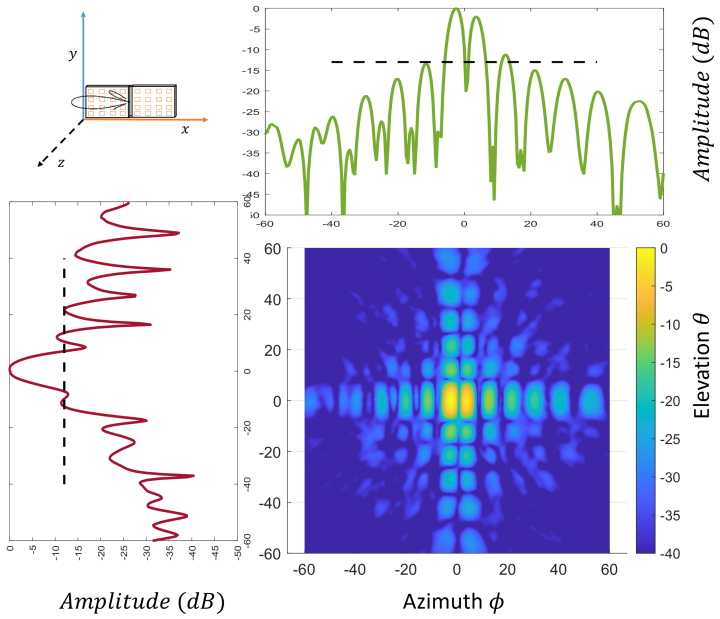

(a)

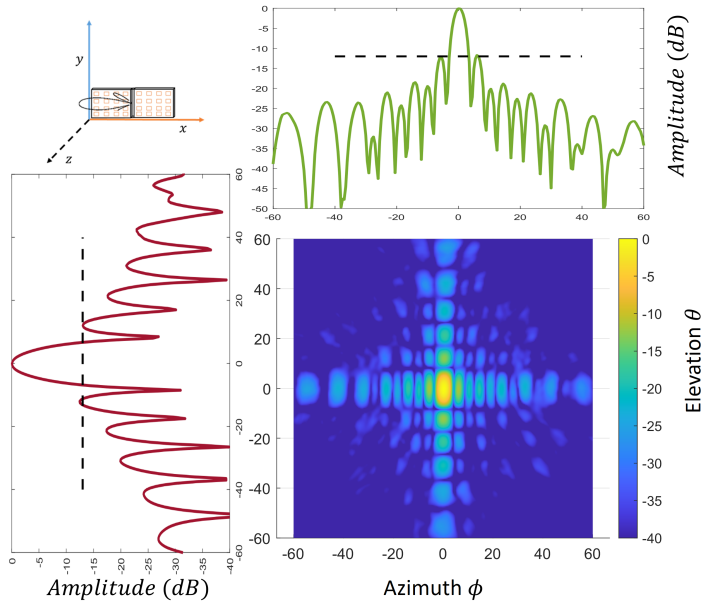

(b)

Figure 5.9: Far-field pattern measurement in the NF chamber for 512 element active phased array (a) uncalibrated pattern measurement and (b) is the calibrated pattern measurement with the black dashed line for −13 dB side-lobe level.

phase offset is introduced to generate the uncalibrated pattern. The uncalibrated phase in Figure 5.10 shows the difference between two panels after the manual 180° phase offset. However, after the calibration, the phase pattern is aligned between the panels. This is also true for the amplitude hologram. The dead elements are also visible in Figure 5.10, which confirms the validation of the quasi-near-field range measurements. The equation used for the RMSE

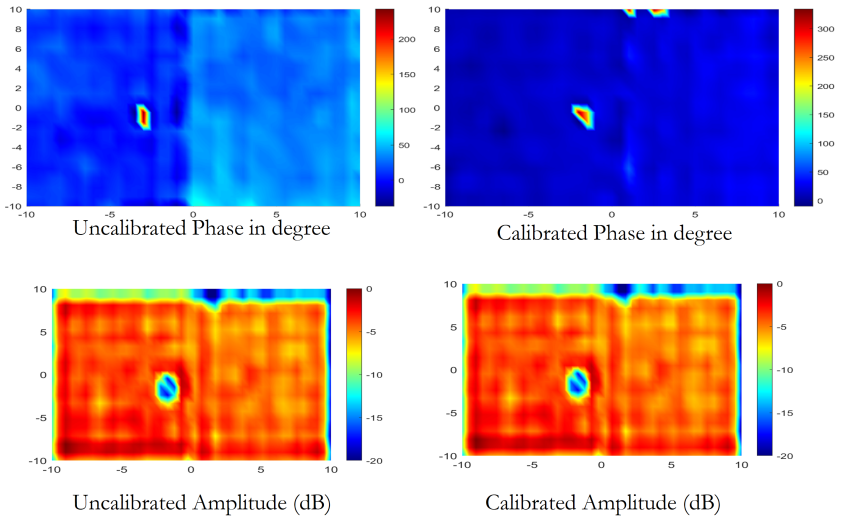

Figure 5.10: Calibrated and uncalibrated Hologram of Phase and amplitude of the AUT in the x axis. Here the 180° phase offset manually included in the uncalibrated phase hologram

calculation is given by

$$RMSE = \sqrt{\frac{\sum_{n=1}^{N}(x_i - x_a)^2}{N}} \ . \tag{5.1}$$

Here x_i is the individual response, and x_a is the average response. For this calculation, the dead elements and the panel gaps are excluded. From Figure 5.10, it is visible that there are some dead elements in the panel. If dead elements are not excluded, then the RMS error value will be skewed. From the data, the RMS error for uncalibrated amplitude was found 3.16 dB, whereas,

for calibrated data, the RMS error was 1.6 dB, which is a significant improvement after calibration. Also, when calculating phase, RMS error of 14.4° is calculated for uncalibrated hologram compare to 8.55° for the calibrated hologram. This improvement in RMSE error is significant. In Figure 5.11b, the directivity versus frequency is plotted for both calibrated and uncalibrated gain pattern. The increase of directivity in the calibrated pattern over the uncalibrated pattern is evident and in the order of 0.5 dB.

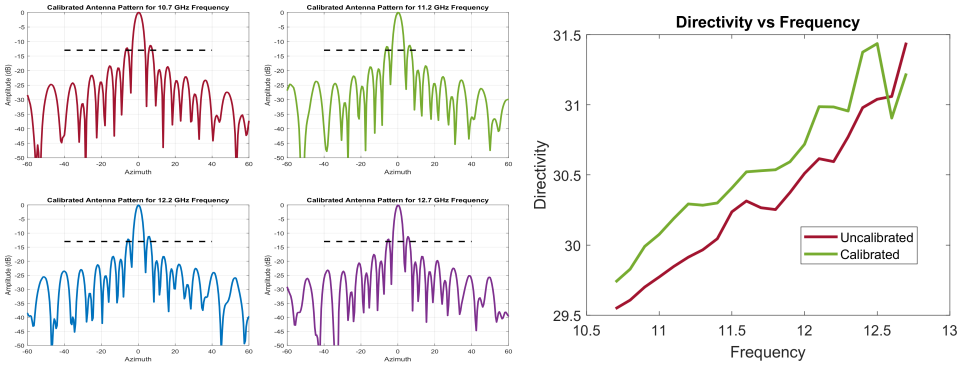

(a) (b)

Figure 5.11: Antenna characteristics (a) far-field pattern in the boresight of the AUT for four different frequency, where the black dashed line depicts the -13 dB SLL line and (b) Frequency versus Directivity plot for the frequency range of $10.7 - 12.7$ GHz. Both calibrated and uncalibrated is showing for comparison

Finally, a plot of the far-field pattern across the frequency is created to observe how efficiently it can hold the calibration across the frequency. The calibration weights were generated for 11.7 GHz frequency. However, the frequency range for the NF chamber was $10.7 - 12.7$ GHz. So the 4 frequency point to observe the far-field pattern are chosen. The frequency points are $10.7, 11.2, 12.2,$ and 12.7 GHz. These frequency points cover the frequency sweep range of $10.7 - 12.7$ GHz. Figure 5.11a shows that the calibration weights hold the far-field pattern strongly in the wide range of frequency,

which is highly desirable.

5.4 Chapter Summary

This chapter plays a vital role in this dissertation as it contains the measured data from the prototype developed and validates the measurements in the near-field range. First, the AUT was calibrated using a fixed probe in the quasi-near-field range. Beam scanning, SLL tapering, and holograms are also shown after calibration of the antenna to prove the calibration standard. Second, the AUT was also tested in the NF chamber since this is a widely accepted antenna measurement process. The NF chamber measurements are aligned with the quasi-near-field range measurements, which validates the proposed technique. The capability of dead element detection was also proved. Finally, with the content of this chapter, it is safe to declare that the proposed method is acceptable for fast calibration techniques. In the next chapter, a summary will be provided as a conclusion. Potential future work will also be discussed.

Chapter 6

Conclusions and Future Work

6.1 Conclusions

This dissertation has detailed the effort to implement fast calibration technique for phased array antenna using a fixed probe in the quasi-near-field. This work is motivated by the increasing demand for fast calibration technique in the aerospace, autonomous vehicle, satellite communication and many other similar industries. This research contributed to valuable experimental results which are of great interest to both industry and academia.

With the development and emergence of low-cost technology, phased array systems are getting very popular nowadays. Many military and commercial applications are perfect candidates for phased array systems. In general, all phased arrays, irrespective of their architecture, need to be calibrated. Once an array is fabricated, it comes with some systematic and random errors. These need to be appropriately addressed before the array is deployed for the operation. Systematic errors are more harmful than random errors. To address the systematic errors and make the array beams in desired shape, an initial calibration is needed right after fabrication and before deploying the array.

Also, there are many random errors generated from secondary parameters during the array operation, which are also needed to be addressed. Therefore, the array needs to be monitored while in operation, which is called in-situ calibration. Depending on the operation, it is not feasible to allow extensive downtime for calibration purposes. This is where the need came up for getting a fast calibration technique.

6.1.1 Dissertation Summary

There is no single calibration technique that fits all systems. The literature on calibration techniques is vast and depending on the system varied widely. Chapter 2 provides a useful exhaustive literature review for available calibration technique. This chapter covers both initial and in-situ calibration techniques using either dedicated internal hardware or external hardware and tools. This chapter categorizes initial versus in-situ, external vs. internal, far-field vs. near-field and dedicated instrument vs. external hardware type calibration procedure. Among them, the NF park and probe technique are most straight forward and most time-consuming. Also, some other novel promising technologies such as REV, Mutual Coupling technique, code-based calibration technique. As discussed earlier, this dissertation's focus is to provide fast calibration that essentially needs a novel idea over these existing techniques to support airborne satellites and satellite ground station antenna. Systems that do not have the luxury to accommodate massive downtime and simultaneously have the option to attach a fixed probe in the quasi-near-field.

Chapter 3 started to address this problem and lay down the theory of fixed probe-based one-shot calibration procedure. The framework was presented, and a detailed mathematical model is proposed for better understanding. This

approach can accommodate both analog and digital phased arrays. However, for a digital phased array, one can get the element level excitation without any computation for their architecture design. However, with an analog array, it is not possible because of the low SNR level. CCE based approach also described displaying its uniqueness. CCE acts very accurately within a limit of erroneous phase shifters and attenuators. Also, the RF system is always prone to leakage errors. A mathematical model of leakage was also presented.

Since the mathematical framework has been introduced, it was time for simulating the proposed technique. Chapter 4 a ®Matlab based sand-box has been prepared to analyze the whole framework. The sand-box can generate the whole system S parameters to account for the mutual coupling, including the probe in front of the AUT. We then simulate the ground truth, uncalibrated pattern, and calibrated pattern. This chapter provides the foundation and motivation for going to the actual measurement.

Finally, in Chapter 5, the measurement was done to validate the proposed model. This part is mostly done at Cedar Rapids, Iowa at Collins Aerospace R&D using one of their ground station user terminal system. Since the system is proprietary to Collins Aerospace, in this dissertation, no specific details are provided. Nevertheless, the measurements were taken in a compact box using a near-field probe to generate calibration weights and tested in their NF range to ensure the process is working. In the end, we have an excellent agreement between the theory, simulation, and measurement.

The advantage of this technique is a fast, low cost, compact range and accurate measurement. This will definitely open new avenues for the phased array calibration as now the maximum time needed to generate calibration weights are in the order of fifteen to twenty minutes. This technique is applicable

for both analog and digital phased array for initial calibration. This is also applicable for in-situ calibration of full digital arrays if it can accommodate a fixed probe in front of the array.

6.1.2 Future Work

There are a couple of things left for future work. This system is developed for single-polarization. A dual-polarized fast calibration approach will be next step. This technique can be applied on unmanned aerial vehicle phased array calibration. Next, the error analysis would be another avenue to explore. This technique is already applied for analog phased arrays but the performance of this calibration can be explored on full digital arrays.

A mathematical framework is developed for addressing the leakage of the system. It can be expanded to the different antenna system to quantify ripples on element pattern. Especially to examine how the alignment error will translate into pattern and calibration error is essential. This technique can also be extended to wide-band arrays.

Finally, it is possible to make the system almost real-time, in the order of 100 millisecond. For a high mutual coupling antenna, this process would not work very well as the orthogonality cannot be maintained in that environment is another area to explore. In a nutshell, there is ample opportunity to explore this novel procedure.

Bibliography

[1] Eli Brookner. "Phased-array and radar breakthroughs". In: *IEEE National Radar Conference - Proceedings* (2007), pp. 37–42. DOI: 10.1109/RADAR.2007.374187.

[2] Eli Brookner. "Radar and phased-array breakthroughs - An update". In: *IET Conference Publications* 2015.CP677 (2015), pp. 26–30. DOI: 10.1049/cp.2015.1300.

[3] Eli Brookner. "Never ending saga of phased array breakthroughs". In: *IEEE International Symposium on Phased Array Systems and Technology* (2010), pp. 61–73. DOI: 10.1109/ARRAY.2010.5613392.

[4] Tony Azar. "Error analysis of tiled overlapped subarrays". In: *2012 2nd International Conference on Advances in Computational Tools for Engineering Applications, ACTEA 2012* (2012), pp. 52–56. DOI: 10.1109/ICTEA.2012.6462902.

[5] Liang Wen, Tao Zeng, and Xiao Liang Li. "Error analysis in phased array antenna pattern simulation". In: *ICCET 2010 - 2010 International Conference on Computer Engineering and Technology, Proceedings* 6 (2010), pp. 287–290. DOI: 10.1109/ICCET.2010.5486245.

[6] Slavko Rupcic and Vanja Mandric. "Effect of experimental model errors on radiation pattern of a spherical aperture antennas array". In:

Proceedings Elmar - International Symposium Electronics in Marine 2.September (2008), pp. 617–620. ISSN: 13342630.

[7] Robert J Mailloux. *Phased array antenna handbook*. Artech house, 2017.

[8] David F Kelley and Warren L Stutzman. "Array antenna pattern modeling methods that include mutual coupling effects". In: *IEEE Transactions on antennas and propagation* 41.12 (1993), pp. 1625–1632.

[9] Joseph K Mulcahey and Michael G Sarcione. "Calibration and diagnostics of the THAAD solid state phased array in a planar nearfield facility". In: *Proceedings of International Symposium on Phased Array Systems and Technology*. IEEE. 1996, pp. 322–326.

[10] David M Pozar. "The active element pattern". In: *IEEE Transactions on Antennas and Propagation* 42.8 (1994), pp. 1176–1178.

[11] David M Pozar. "A relation between the active input impedance and the active element pattern of a phased array". In: *IEEE Transactions on Antennas and Propagation* 51.9 (2003), pp. 2486–2489.

[12] Hans Steyskal and Jeffrey S Herd. "Mutual coupling compensation in small array antennas". In: *IEEE Transactions on Antennas and Propagation* 38.12 (1990), pp. 1971–1975.

[13] DR Fuhrmann. "Estimation of sensor gain and phase using known field covariance". In: *Acoustics, Speech, and Signal Processing, IEEE International Conference on*. IEEE Computer Society. 1991, pp. 1369–1372.

[14] MA Koerber and DR Fuhrmann. "Array calibration by Fourier series parameterization: Stochastic maximum likelihood solution". In: *[1992] IEEE Sixth SP Workshop on Statistical Signal and Array Processing*. IEEE. 1992, pp. 304–307.

[15] Frank C Robey, Daniell R Fuhrmann, and SI Krich. "Array calibration utilizing clutter scattering". In: *IEEE Seventh SP Workshop on Statistical Signal and Array Processing*. IEEE. 1994, pp. 317–320.

[16] Jason Yu and Jeffrey Krolik. "Adaptive phase-array calibration using MIMO radar clutter". In: *2013 IEEE Radar Conference (RadarCon13)*. IEEE. 2013, pp. 1–5.

[17] Caleb Fulton et al. "Digital phased arrays: Challenges and opportunities". In: *Proceedings of the IEEE* 104.3 (2016), pp. 487–503.

[18] John Ambrose Fleming. *The principles of electric wave telegraphy and telephony*. Longmans, Green, 1919.

[19] HT Friis. "A new directional receiving system". In: *Proceedings of the Institute of Radio Engineers* 13.6 (1925), pp. 685–707.

[20] Harald T Friis and Carl B Feldman. "A multiple unit steerable antenna for short-wave reception". In: *Proceedings of the Institute of Radio Engineers* 25.7 (1937), pp. 841–917.

[21] Stone John Stone. *Directive antenna array*. US Patent 1,643,323. Sept. 1927.

[22] GH Brown. "Directional antennas". In: *Proceedings of the institute of radio engineers* 25.1 (1937), pp. 78–145.

[23] E Sharp. "A triangular arrangement of planar-array elements that reduces the number needed". In: *IRE Transactions on Antennas and Propagation* 9.2 (1961), pp. 126–129.

[24] Georges A Deschamps. "Microstrip microwave antennas". In: *Proceedings of the Third Symposium on the USAF Antenna Research and Development Program, Oct*. 1953, pp. 18–22.

[25] Robert Munson. "Microstrip phased array antennas". In: *1973 EIC 11th Electrical Insulation Conference*. IEEE. 1973, pp. 281–283.

[26] PJ Gibson. "The vivaldi aerial". In: *1979 9th European Microwave Conference*. IEEE. 1979, pp. 101–105.

[27] Mark E Weber et al. "The next-generation multimission US surveillance radar network". In: *Bulletin of the American Meteorological Society* 88.11 (2007), pp. 1739–1752.

[28] Michele Galletti et al. "CPPAR-Cylindrical polarimetric phased array radar system design". In: *2011 IEEE RadarCon (RADAR)*. IEEE. 2011, pp. 033–038.

[29] Nicholas Peccarelli et al. "Survey: Characterization and mitigation of spatial/spectral interferers and transceiver nonlinearities for 5G MIMO systems". In: *IEEE Transactions on Microwave Theory and Techniques* 67.7 (2019), pp. 2829–2846.

[30] Erik G Larsson et al. "Massive MIMO for next generation wireless systems". In: *IEEE communications magazine* 52.2 (2014), pp. 186–195.

[31] Constantine A Balanis. *Antenna theory: analysis and design*. John wiley & sons, 2016.

[32] Rafael H Medina-Sanchez. "Beam Steering Control System for Low-Cost Phased Array Weather Radars: Design and Calibration Techniques". In: (2014).

[33] Yuen T Lo and SW Lee. *Antenna Handbook: theory, applications, and design*. Springer Science & Business Media, 2013.

[34] Robert C Hansen. *Phased array antennas*. Vol. 213. John Wiley & Sons, 2009.

[35] Robert E Collin and Francis J Zucker. "Antenna theory". In: (1969).

[36] L Rondinelli. "Effects of random errors on the performance of antenna arrays of many elements". In: *1958 IRE International Convention Record*. Vol. 7. IEEE. 1966, pp. 174–189.

[37] K Carver, W Cooper, and W Stutzman. "Beam-pointing errors of planar-phased arrays". In: *IEEE Transactions on Antennas and Propagation* 21.2 (1973), pp. 199–202.

[38] Bernard D Steinberg. "Principles of aperture and array system design: Including random and adaptive arrays". In: *wi* (1976).

[39] GHC Van Werkhaven and AKd Golshayan. "Calibration aspects of the APAR antenna unit". In: *Proceedings 2000 IEEE International Conference on Phased Array Systems and Technology (Cat. No. 00TH8510)*. IEEE. 2000, pp. 425–428.

[40] Caleb J Fulton. "Digital array radar calibration and performance monitoring techniques for direct conversion and dual polarization architectures". PhD thesis. Purdue University, 2011.

[41] M Sarcione et al. "The design, development and testing of the THAAD (Theater High Altitude Area Defense) solid state phased array (formerly ground based radar)". In: *Proceedings of International Symposium on Phased Array Systems and Technology*. IEEE. 1996, pp. 260–265.

[42] Wolfgang Haselwander et al. “Measurement on an active phased array antenna on a near-field range and an anechoic far-field chamber”. In: *2001 31st European Microwave Conference*. IEEE. 2001, pp. 1–5.

[43] Gregory Sadowy et al. “UAVSAR Active Electronically-Scanned Array”. In: *2010 IEEE International Symposium on Phased Array Systems and Technology*. IEEE. 2010, pp. 763–770.

[44] Rafael H Medina et al. “Calibration and validation of the CASA phased array antenna”. In: *2012 42nd European Microwave Conference*. IEEE. 2012, pp. 940–943.

[45] Willard T Patton and Leonard H Yorinks. “Near-field alignment of phased-array antennas”. In: *IEEE Transactions on Antennas and Propagation* 47.3 (1999), pp. 584–591.

[46] Alan J Fenn. *Adaptive antennas and phased arrays for radar and communications*. Artech House, 2007.

[47] JGV Hezewijk. “Fast determination of the element excitation of active phased array antennas”. In: *IEEE AP-S Int. Symp. Digest*. 1991, pp. 1478–1481.

[48] Herbert M Aumann and Francis G Willwerth. *Phased-Array Calibration by Adaptive Nulling*. Tech. rep. MASSACHUSETTS INST OF TECH LEXINGTON LINCOLN LAB, 1991.

[49] Cheng-Nan Hu. “A novel method for calibrating deployed active antenna arrays”. In: *IEEE Transactions on Antennas and Propagation* 63.4 (2015), pp. 1650–1657.

[50] Caleb Fulton et al. “Cylindrical polarimetric phased array radar: Beamforming and calibration for weather applications”. In: *IEEE Transactions on Geoscience and Remote Sensing* 55.5 (2017), pp. 2827–2841.

[51] Igor Ivić et al. “An Overview of Weather Calibration for the Advanced Technology Demonstrator”. In: *2019 IEEE International Symposium on Phased Array System & Technology (PAST)*. IEEE. 2019, pp. 1–7.

[52] Seiji Mano and Takashi Katagi. “A method for measuring amplitude and phase of each radiating element of a phased array antenna”. In: *Electronics and Communications in Japan (Part I: Communications)* 65.5 (1982), pp. 58–64.

[53] Toru Takahashi et al. “Theoretical study on measurement accuracy of rotating element electric field vector (REV) method”. In: *Electronics and Communications in Japan (Part I: Communications)* 89.1 (2006), pp. 22–33.

[54] Toru Takahashi, Yoshihiko Konishi, and Isamu Chiba. “A novel amplitude-only measurement method to determine element fields in phased arrays”. In: *IEEE transactions on antennas and propagation* 60.7 (2012), pp. 3222–3230.

[55] Minggang Liu and Zhenghe Feng. “Combined rotating-element electric-field vector (CREV) method for nearfield calibration of phased array antenna”. In: *2007 International Conference on Microwave and Millimeter Wave Technology*. IEEE. 2007, pp. 1–4.

[56] Rui Long et al. “Fast amplitude-only measurement method for phased array calibration”. In: *IEEE transactions on antennas and propagation* 65.4 (2016), pp. 1815–1822.

[57] Thomas Moon, Junfeng Gaun, and Haitham Hassanieh. "Online millimeter wave phased array calibration based on channel estimation". In: *2019 IEEE 37th VLSI Test Symposium (VTS)*. IEEE. 2019, pp. 1–6.

[58] XueFei Zheng, Tie Gao, and XueLi Chen. "Mid-field calibration technique of active phased array antennas". In: *2005 Asia-Pacific Microwave Conference Proceedings*. Vol. 3. IEEE. 2005, 4–pp.

[59] Qiang Gu et al. "Analysis of amplitude-phase error of phased array calibration in mid-field". In: *Proceedings of 2014 3rd Asia-Pacific Conference on Antennas and Propagation*. IEEE. 2014, pp. 280–283.

[60] Ruoxin Li et al. "An accurate mid-field calibration technique for large phased array antenna". In: *2017 Sixth Asia-Pacific Conference on Antennas and Propagation (APCAP)*. IEEE. 2017, pp. 1–3.

[61] Daniel S Purdy. "An automated process for efficiently measuring the patterns of all elements located in a phased-array antenna". In: *Proceedings 2000 IEEE International Conference on Phased Array Systems and Technology (Cat. No. 00TH8510)*. IEEE. 2000, pp. 521–524.

[62] Seth D Silverstein. "Algorithms for remote calibration of active phased array antennas for communication satellites". In: *Conference Record of The Thirtieth Asilomar Conference on Signals, Systems and Computers*. IEEE. 1996, pp. 1181–1185.

[63] Erik Lier et al. "Phased array calibration and characterization based on orthogonal coding: Theory and experimental validation". In: *2010 IEEE International Symposium on Phased Array Systems and Technology*. IEEE. 2010, pp. 271–278.

[64] Shuo Wang, Haiming Qi, and Weidong Yu. "Polarimetric SAR internal calibration scheme based on T/R module orthogonal phase coding". In: *IEEE transactions on geoscience and remote sensing* 47.12 (2009), pp. 3969–3980.

[65] Benjamin Brautigam et al. "Individual T/R module characterisation of the TerraSAR-X active phased array antenna by calibration pulse sequences with orthogonal codes". In: *2007 IEEE International Geoscience and Remote Sensing Symposium*. IEEE. 2007, pp. 5202–5205.

[66] Harold Shnitkin. "Rapid fast Fourier transform phase alignment of an electronically scanned antenna". In: *1990 20th European Microwave Conference*. Vol. 1. IEEE. 1990, pp. 247–251.

[67] Toru Takahashi et al. "Fast measurement technique for phased array calibration". In: *IEEE Transactions on Antennas and Propagation* 56.7 (2008), pp. 1888–1899.

[68] VA Usin et al. "Automatic diagnostic and alignment in phased array antennas". In: *MMET Conference Proceedings. 1998 International Conference on Mathematical Methods in Electromagnetic Theory. MMET 98 (Cat. No. 98EX114)*. Vol. 2. IEEE. 1998, pp. 591–593.

[69] Dave Bekers, Raymond van Dijk, and Frank van Vliet. "Mutual-coupling based phased-array calibration: A robust and versatile approach". In: *2013 IEEE International Symposium on Phased Array Systems and Technology*. IEEE. 2013, pp. 630–637.

[70] Guolong He, Xin Gao, and Hui Zhou. "Fast Phased Array Calibration by Power-Only Measurements Twice for Each Antenna Element". In: *International Journal of Antennas and Propagation* 2019 (2019).

[71] Herbert M Aumann, Alan J Fenn, and Frank G Willwerth. "Phased array antenna calibration and pattern prediction using mutual coupling measurements". In: *IEEE Transactions on Antennas and Propagation* 37.7 (1989), pp. 844–850.

[72] J Herd. "Experimental results from a self-calibrating digital beamforming array". In: *International Symposium on Antennas and Propagation Society, Merging Technologies for the 90's*. IEEE. 1990, pp. 384–387.

[73] Ashok Agrawal and Allan Jablon. "A calibration technique for active phased array antennas". In: *IEEE International Symposium on Phased Array Systems and Technology, 2003.* IEEE. 2003, pp. 223–228.

[74] M Lanne et al. "Wideband array antenna system development". In: *2010 IEEE International Symposium on Phased Array Systems and Technology*. IEEE. 2010, pp. 789–795.

[75] Kuan-Min Lee, Ruey-Shi Chu, and Sien-Chang Liu. "A built-in performance-monitoring/fault isolation and correction (PM/FIC) system for active phased-array antennas". In: *IEEE transactions on antennas and propagation* 41.11 (1993), pp. 1530–1540.

[76] Grant A Hampson and A Bert Smolders. "A fast and accurate scheme for calibration of active phased-array antennas". In: *IEEE Antennas and Propagation Society International Symposium. 1999 Digest. Held in conjunction with: USNC/URSI National Radio Science Meeting (Cat. No. 99CH37010)*. Vol. 2. IEEE. 1999, pp. 1040–1043.

[77] Achim Dreher et al. "Antenna and receiver system with digital beamforming for satellite navigation and communications". In: *IEEE Trans-*

actions on Microwave Theory and Techniques 51.7 (2003), pp. 1815–1821.

[78] Daniel J Rabideau et al. "An S-band digital array radar testbed". In: *IEEE International Symposium on Phased Array Systems and Technology, 2003.* IEEE. 2003, pp. 113–118.

[79] Erik Lier and Anthony Jacomb-Hood. "Deployed and modular active phased array satellite antenna". In: *18th International Communications Satellite Systems Conference and Exhibit.* 2000, p. 1253.

[80] Seth D Silverstein. "Application of orthogonal codes to the calibration of active phased array antennas for communication satellites". In: *IEEE transactions on signal processing* 45.1 (1997), pp. 206–218.

[81] Daniel S Purdy and Anthony Jacomb-Hood. "In orbit active array calibration for NASA's LightSAR". In: *Proceedings of the 1999 IEEE Radar Conference. Radar into the Next Millennium (Cat. No. 99CH36249).* IEEE. 1999, pp. 172–176.

[82] D Purdy, J Ashe, and G Kautz. "Experimental verification of the CCE technique for calibration of phased arrays". In: *Antenna Measurement and Techniques Association Symposium (AMTA).* 1999.

[83] Erik Lier et al. "An on-board integrated beam conditioning system for active phased array satellite antennas". In: *Proceedings 2000 IEEE International Conference on Phased Array Systems and Technology (Cat. No. 00TH8510).* IEEE. 2000, pp. 509–512.

[84] Krishnasamy T Selvan and Ramakrishna Janaswamy. "Fraunhofer and Fresnel Distances: Unified derivation for aperture antennas." In: *IEEE Antennas and Propagation Magazine* 59.4 (2017), pp. 12–15.

[85] Carlton H Walter. *Traveling wave antennas*. Dover Publications,[1970, 1970.

[86] Bernhard E Keiser. "Principles of electromagnetic compatibility". In: *ah* (1979).

[87] Donald RJ White. "EMI control methods and techniques". In: (1981).

[88] Arthur Yaghjian. "An overview of near-field antenna measurements". In: *IEEE Transactions on antennas and propagation* 34.1 (1986), pp. 30–45.

[89] Gregory Michael Kautz, Jeffrey Michael Ashe, and Seth David Silverstein. *Method and apparatus for calibrating a remote system which employs coherent signals*. US Patent 6,384,781. May 2002.

[90] Erik Lier, Daniel Sanford Purdy, and Gregory Michael Kautz. *Calibration and integrated beam control/conditioning system for phased-array antennas*. US Patent 6,163,296. Dec. 2000.

[91] M Nhat Pham, Ridvan Akpinar, and Arne F Jacob. "Probe-receiver coupling in external calibration systems". In: *2016 German Microwave Conference (GeMiC)*. IEEE. 2016, pp. 409–412.

[92] M Nhat Pham and Arne F Jacob. "Mutual coupling compensation of a DBF receiver array". In: *2015 European Microwave Conference (EuMC)*. IEEE. 2015, pp. 722–725.

[93] RUDOLF Becchmann. "On the calculation of radiation resistance of antennas and antenna combinations". In: *Proceedings of the Institute of Radio Engineers* 19.8 (1931), pp. 1471–1480.

[94] Shajid Islam and Caleb Fulton. "Fixed Probe Based One-Shot Calibration Technique for Small Digital Phased Array". In: *2019 IEEE International Symposium on Phased Array System & Technology (PAST)*. IEEE. 2019, pp. 1–5.

[95] Shajid Islam and Caleb Fulton. "Fixed Probe Based Digital Phased Array Calibration Using Virtual Probe Location". In: *2020 IEEE International Radar Conference (RADAR)*. IEEE. 2020, pp. 792–797.

[96] A Balanis Constantine. *Antenna theory: analysis and design*. Wiley-Interscience, 2005.

[97] Chen Wu. "Analysis of finite parallel-plate waveguide arrays". In: *IEEE Transactions on Antennas and Propagation* 18.3 (1970), pp. 328–334.

[98] Caleb Fulton et al. "Polarimetrie phased array calibration for large-scale multi-mission radar applications". In: *2018 IEEE Radar Conference (RadarConf18)*. IEEE. 2018, pp. 1272–1277.

[99] Stuart Gregson, John McCormick, and Clive Parini. *Principles of planar near-field antenna measurements*. Vol. 53. IET, 2007.

[100] Dan Slater. *Near-field antenna measurements*. Artech House, 1991.

[101] Andrew G Repjar, Allen C Newell, and Michael H Francis. "Accurate determination of planar near-field correction parameters for linearly polarized probes". In: *IEEE Transactions on Antennas and Propagation* 36.6 (1988), pp. 855–868.

[102] David M Kerns. "Plane-wave scattering-matrix theory of antennas and antenna-antenna interactions-Formulation and applications". In: *JResB* 80 (1976), pp. 5–51.

[103] Frank Boldissar and Amanuel Haile. “Near Field Measurement Errors Due To Neglecting Probe Cross-Polarization”. In: *AMTA Symposium Digest*. 2007, pp. 3–7.

[104] Gregory F Masters and Stuart F Gregson. “Coordinate system plotting for antenna measurements”. In: *AMTA Annual Meeting & Symposium*. 2007.

[105] Nafati A Aboserwal et al. “Source current polarization impact on the cross-polarization definition of practical antenna elements: Theory and applications”. In: *IEEE Transactions on Antennas and Propagation* 66.9 (2018), pp. 4391–4406.

Appendix A

Near Field Measurement

A.1 Near Field Planar System

Ideally antenna patterns should be measured by having an ideal plane wave source/receiver, rotating the AUT to the angular coordinates of interest and sampling the received signal at each position. A typical example of this is a Far-Field (FF) test, where the AUT is positioned far enough from an antenna probe, and the AUT is rotated to capture its antenna pattern at different angles. This is called a direct measurement, because the long probe-to-AUT distance directly collimates the radiated waves [99]. Other direct methods involve using lenses and/or reflective surfaces, as in compact antenna test ranges. On the other hand, for electrically large AUTs where the FF distance may be simply too large to arrange a direct test type, an indirect measurement is more convenient. Indirect methods are often tests that sample the AUT at its NF region, and later post-process the antenna patterns to a FF distances. Since the NF region is just a few wavelengths away from the AUT, shorter distances are needed and smaller chambers can be used.

NF tests are typically performed by planar, cylindrical and spherical sys-

tems, mainly because the required robotic mechanical scanners are relatively easy to build, and convenient mathematical approaches can be applied to process FF data from the sampled NF data, i.e., the Helmholtz equation is separable on these coordinate systems. Each system has its own advantages over the others; planar scans are used on high-gain antennas, spherical on omnidirectional antennas, and cylindrical on fan beam antennas. A list of the main differences can be found in Table A.1, which clearly indicates that, to characterize, a high-gain antenna like the LRU, the suitable scan configuration should be planar.

Parameter	Planar	Cylindrical	Spherical
High-gain	excellent	good	good
Low-gain	poor	poor	excellent
Probe correction	simple	complex	complex
Speed	fast	slow	slow
Alignment	easy	difficult	more difficult

Table A.1: NF scan types classification, main differences and advantages. Source: [100]

The NF planar scanner used in this project is located at the Radar Innovation Laboratory, and was manufactured by NSI. The dimensions of its scanning windows are a horizontal span of 62.46 in, vertical of 62.46 in, and a short course of 4 in of transverse movement, which is used to finely adjust the probe-to-AUT distance. The window dimension defines the maximum FF angle range that can be measured, i.e., the larger the window, the wider the FF range that can be processed. The relation can be expressed as [100]

$$H = D + P + 2Ztan\theta, \tag{A.1}$$

where H is the scan height, D is the antenna aperture height, P is the probe height, Z is the probe-to-AUT distance, and θ is the maximum FF angle that

can be accurately calculated. There is not enough information from the scan to obtain the pattern at angles $> |\theta|$ away from the boresight axis. For this project the values of H, D, P, Z, and θ are given. Notice that θ was defined as 65° because often there is no need to have information on the steering capability of a phased array above 45°, and also a smaller angle results in a smaller scan height, which also translates to a lower scan time. The value of H was calculated for $\theta = 65°$.

Symbol	Magnitude	Value	Unit
D	Antenna aperture height	9	in
P	Probe height	1.872	in
H	Scan height	43.31	in
Z	Probe to AUT distance	7.57	in

Table A.2: Definition of the NF scan parameters

A.2 NF Probe Correction

All NF tests require the use of an antenna probe, and due to the fact that all antennas have their own radiation pattern, the data sampled by the probe is influenced by its own radiation. Hence, an essential step to process the FF patterns from NF sampled data is probe correction, which analytically removes the effect of the probe from the calculated FF pattern. An in depth revision of the theory behind planar NF to FF transformation is given by [101, 102]. The scans for this project were performed using a WR-187 open ended waveguide (OEWG).

In the case of planar NF, the probe correction is a straightforward procedure. However, as will be explained later, despite its relative simplicity, the accuracy of the technique to process the cross-polarization pattern is poor.

The full probe correction in planar scans requires a deep knowledge of the co- and cross-polarization patterns of the probe, which, for an OEWG, are a broad beam for the co-, and a lower power beam with a narrow null along the principal planes for the cross-polarization. Moreover, the alignment of the probe with respect to the AUT is crucial to the procedure. The boresight axes of both antennas should always be parallel, since any deviation will incur a systematic error and preclude the correct FF computation.

The mentioned misalignment issue is especially problematic for the computation of the cross-polarization pattern of the AUT, which is heavily affected by the nature of the inherent cross-polarization of the probe. Since the cross-polarization pattern has a narrow null, any misalignment will misplace a deep null in a position where a higher signal was expected, rendering errors to the computation of the cross pattern of the AUT. Furthermore, it is not common to have an accurate measurement of the co- and cross-polarization patterns of the probe. However, due to its simple radiating mechanism the co-pattern is usually calculated, either analytically or by simulation, with sufficient accuracy.

Commercial scanners often employ an approximate technique instead of the full probe correction. The approximation assumes that the co-polarization is much larger than its cross counter-part, and simply neglects its value during the pattern correction. This approximation works very well for co-pattern computation, with errors <0.1 dB, although the cross-polarization may have errors of 3dB when using an OEWG with -40dB cross-polarization nulls to measure an AUT as APAR with -30dB level cross-polarization [103]. For this project, the probe correction was performed using the scanner software, which employs the approximated probe correction.

A.3 Coordinate System and Polarization

The representation of an antenna pattern consists of quantifying the electric or magnetic vector fields over a section of the spatial domain. Usually, one plots the tangential components of the fields of the FF pattern at a finite number of sample points. The sample points are represented according to the selected coordinate system, and the tangential components, often named co- and cross-components, are represented according to the selected polarization. A great summary of this topic can be found in [104].

According with [104], for micro-strip antennas the Ludwig second definition is more suitable to display the patterns, because the the cross polarization component is closer this definition rather than the third one. For this reason all plots shown in this report use Ludwig II polarization. The transformation from second to third definition is straight forward [105].